Appl. Phys. B 68, 1–25 (1999)

Applied Physics B
Lasers
and Optics

Invited paper

Precision spectroscopy with coherent dark states

R. Wynands, A. Nagel

Institut für Angewandte Physik, Universität Bonn, Wegelerstraße 8, D-53115 Bonn, Germany
(Fax: +49-228/733-474, E-mail: wynands@iap.uni-bonn.de)

Received: 14 September 1998

Abstract. Using optical phase-locking and a buffer gas, coherent population trapping resonances with linewidths below 50 Hz can be observed in a thermal cesium vapor. External influences on the cesium multilevel system, such as magnetic fields, laser polarizations and intensities, have been studied and can quantitatively be described by intuitive theoretical models. Based on these investigations we have performed precision measurements, for instance the sensitive detection of magnetic fields in the pT (ac) and nT (dc) range and the determination of g-factor ratios.

PACS: 42.50.Gy; 32.70.Jz; 32.10.Dk

Coherent population trapping, discovered more than twenty years ago by Alzetta et al. [1], has in recent years found application in areas as diverse as laser cooling below the one-photon recoil limit [2], atomic beam frequency standards [3], and in proposed high-sensitivity magnetometry [4, 5]. Coherent population trapping is a resonance phenomenon due to a quantum mechanical interference effect in an atomic system that cancels the absorption of a bichromatic light field. In a suitable level configuration, which can be found, for instance, in alkali atoms, this allows one to probe coherences between long-lived ground states in an all-optical way. The introduction of the optical phase-locking technique, combined with the use of vapor cells containing an additional buffer gas, has recently allowed one to obtain resonance linewidths of less than 50 Hz at good signal-to-noise ratio and stability [6]. Due to the combination of extremely narrow resonances at vanishing absorption with the advantages and the experimental ease of an all-optical device, such a system is a very promising candidate for precision measurements based on the detection of frequency shifts. In fact, a magnetometer with sub-picotesla sensitivity for ac fields has already been constructed [7]. Further improvements in sensitivity might in the long run lead to more sensitive tests of parity and time reversal violation in atomic systems. Other possible applications are a compact primary atomic clock and the determination of the ratio g_I/g_J of nuclear and electronic g-factors.

In order to assess the true potential of coherent population trapping for precision measurements it is essential to understand the system itself and its behavior under a variety of external influences. Accordingly, the focus of this work lies on a detailed study of coherent population trapping in cesium vapor as a function of experimental conditions.

In the first section we will give a brief introduction to the theoretical basis of coherent population trapping in a three-level atomic system. Section 2 will describe the crucial experimental technique used here, optical phase-locking at frequency differences of several GHz, and Sect. 3 will give detailed information on the experiments in cesium vapor including the effects of an additional buffer gas. In Sect. 4 a rather simple method is described that allows one to extend the concept of coherent population trapping from a simple three-level system to the cesium configuration with 32 atomic levels involved. The dark resonances are characterized in detail for arbitrary polarizations and magnetic field directions, and excellent agreement between theory and experiment is found. A collection of important systematic frequency shifting effects – such as the influence of the ac Stark shift – is presented in Sect. 5, together with theoretical models describing them. Suitable operating points for precision applications are identified. Three chapters on specific examples of precision measurements – magnetometry, determination of g-factor ratios, frequency standards – conclude this work.

1 Coherent dark states in Λ systems

Coherent population trapping resonances with a narrow linewidth can occur in systems with two long-lived states $|1\rangle$ and $|2\rangle$ and one excited state $|3\rangle$ coupled by two light fields $E_1 \exp(-\mathrm{i}\omega_1 t - \mathrm{i}\varphi_1)$ and $E_2 \exp(-\mathrm{i}\omega_2 t - \mathrm{i}\varphi_2)$ in an arrangement of energy levels similar to the Greek letter Λ (so-called Λ system, Fig. 1). This configuration is realized, for instance, in the alkali atoms where $|1\rangle$ and $|2\rangle$ can be identified with the two hyperfine components of the ground state and $|3\rangle$ with the first excited level. It is assumed here that each light field interacts with only one of the transitions. According to the definitions $\Delta_{\mathrm{hfs}} = \Omega_2 - \Omega_1$, optical detuning $\delta_{\mathrm{L}} = \omega_2 - \omega_{32}$,

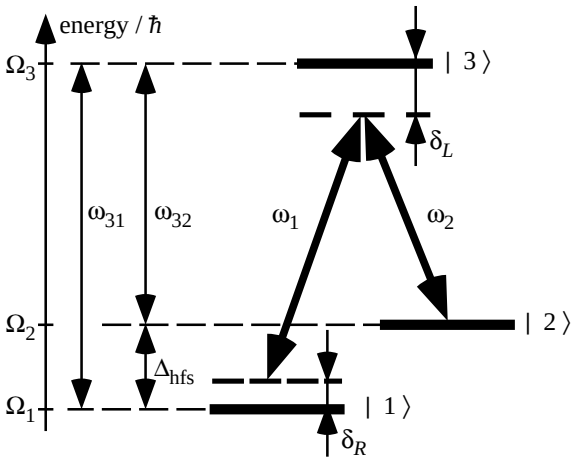

Fig. 1. The three-level Λ system

and Raman detuning $\delta_{\rm R} = (\omega_1 - \omega_2) - \Delta_{\rm hfs}$ the figure shows the case of $\delta_{\rm L} < 0$ and $\delta_{\rm R} < 0$.

If $\omega_2 \approx \omega_{32}$ the population in level $|2\rangle$ can be excited into $|3\rangle$ from where it can decay not only back into $|2\rangle$ but also into $|1\rangle$ (optical pumping). The increased population of $|1\rangle$ leads to a higher absorption of light field 1 as compared to the case of $E_2 = 0$. A similar argument holds for reversed roles of light fields 1 and 2. If, as in the case of a three-level system, the two transitions involve the same excited state an interference effect occurs that reduces the absorption of both fields.

The underlying physics of this process can most easily be seen when the atomic system is described in a different basis. Instead of the energy eigenstates $|1\rangle$ and $|2\rangle$ for an atom at rest the linear combinations $|+\rangle$ and $|-\rangle$ are introduced:

$$|+\rangle = \frac{1}{g_\Lambda}\left(g_1^* |1\rangle + g_2^* |2\rangle\right) , \tag{1}$$

$$|-\rangle = \frac{1}{g_\Lambda}\left(g_2 |1\rangle - g_1 |2\rangle\right) , \tag{2}$$

where the Rabi frequencies g_i are defined in terms of the transition dipole moments:

$$g_1 = -d_{31} E_1/\hbar , \tag{3}$$

$$g_2 = -d_{32} E_2/\hbar , \tag{4}$$

$$g_\Lambda = \sqrt{|g_1|^2 + |g_2|^2} , \tag{5}$$

$$d_{3i} = -e \langle 3| r |i\rangle , \qquad i = 1, 2 . \tag{6}$$

For $\Delta_{\rm hfs} \neq 0$ the new states are noenergy eigenstates but develop in time:

$$|+\rangle(t) = \frac{1}{g_\Lambda} \mathrm{e}^{-\mathrm{i}\Omega_1 t}\left(g_1^* |1\rangle + \mathrm{e}^{-\mathrm{i}\Delta_{\rm hfs} t} g_2^* |2\rangle\right) , \tag{7}$$

$$|-\rangle(t) = \frac{1}{g_\Lambda} \mathrm{e}^{-\mathrm{i}\Omega_1 t}\left(g_2 |1\rangle - \mathrm{e}^{-\mathrm{i}\Delta_{\rm hfs} t} g_1 |2\rangle\right) . \tag{8}$$

In the rotating wave approximation the electric dipole operator coupling ground and excited states is

$$V_{\rm dip} = \frac{\hbar g_1}{2} \exp(-\mathrm{i}\omega_1 t - \mathrm{i}\varphi_1) |3\rangle \langle 1| + \mathrm{c.c.} + \frac{\hbar g_2}{2} \exp(-\mathrm{i}\omega_2 t - \mathrm{i}\varphi_2) |3\rangle \langle 2| + \mathrm{c.c.} \tag{9}$$

so that with $\Delta\varphi = \varphi_1 - \varphi_2$ the transition dipole matrix elements into the excited state are

$$\langle 3| V_{\rm dip} |+\rangle = \frac{\hbar}{2g_\Lambda} \exp[-\mathrm{i}(\Omega_1 + \omega_1)t - \mathrm{i}\varphi_1] \times \left(|g_1|^2 + |g_2|^2 \exp[\mathrm{i}\delta_{\rm R} t + \mathrm{i}\Delta\varphi]\right) , \tag{10}$$

$$\langle 3| V_{\rm dip} |-\rangle = \frac{\hbar g_1 g_2}{2g_\Lambda} \exp[-\mathrm{i}(\Omega_1 + \omega_1)t - \mathrm{i}\varphi_1] \times (1 - \exp(\mathrm{i}\delta_{\rm R} t + \mathrm{i}\Delta\varphi)) . \tag{11}$$

When the difference frequency of the two light fields matches the ground state splitting ($\delta_{\rm R} = 0$) at proper relative phase ($\Delta\varphi = 0$) only transitions starting from $|+\rangle$ are possible:

$$\langle 3| V_{\rm dip} |+\rangle = \frac{\hbar g_\Lambda}{2} \exp[-\mathrm{i}(\Omega_1 + \omega_1)t - \mathrm{i}\varphi_1] , \tag{12}$$

$$\langle 3| V_{\rm dip} |-\rangle = 0 . \tag{13}$$

$|-\rangle$ is called a coherent dark state. Atomic population that is optically pumped out of state $|+\rangle$ becomes trapped in $|-\rangle$ which reduces the fluorescence intensity and makes the medium appear "darker". The process of optical pumping into the coherent dark state is called *coherent population trapping* (CPT) [8,9] or *electromagnetically induced transparency* (EIT) [10] and was first identified in experiments on sodium vapor [1]. It has since been observed in a variety of systems and has been applied to areas as diverse as laser cooling of atoms [2] – acknowledged by a share of the 1997 Nobel prize in physics for C. Cohen-Tannoudji – and isotope separation in optically thick media [11].

The reduction of absorption is due to the destructive interference of the transition amplitudes along the two possible excitation pathways to level $|3\rangle$. The coherent nature of the process manifests itself in the coherent superposition of states in (1) and (2) and in the appearance of the light phases in (10) and (11). If the relative phase of the two light fields changes from $\Delta\varphi = 0$ to $\Delta\varphi = \pi$ the state $|-\rangle$ becomes "bright" while $|+\rangle$ becomes "dark" for equal Rabi frequencies. Therefore in an experiment the relative phase stability of the two light sources plays a crucial role.

In a more realistic model one has to introduce dephasing and decay constants for all levels. The standard way to describe the system is the density matrix formalism using the original energy eigenstates as basis. The coherent superpositions in (1) and (2) are then replaced by ground state coherences, i.e., a non-zero off-diagonal density matrix element ρ_{12}. The solution of the equations of motion for the density matrix ρ in the steady state allows one to calculate the complex susceptibility of the medium near the Raman resonance, for instance for fixed $\omega_2 = \omega_{32}$ and variable ω_1. In a recently published review article by Arimondo [12] this standard treatment is shown and many references to related articles are given. For example, an analytical formula has been derived by Kelley et al. [13] for a number of special cases. Using computer algebra Grishanin et al. [14] obtained a fully analytic solution for the population in the excited state of a Λ system in the rotating wave approximation. It takes the form of a rational function of $\delta_{\rm L}$ and $\delta_{\rm R}$:

$$n_3 = \frac{A\delta_{\rm R}^2 + B}{C\delta_{\rm R}^4 + 2C\delta_{\rm L}\delta_{\rm R}^3 + (D + E\delta_{\rm L}^2)\delta_{\rm R}^2 + F\delta_{\rm L}\delta_{\rm R} + G\delta_{\rm L}^2 + H} , \tag{14}$$

with coefficients

$$
\begin{aligned}
A &= 8\Gamma_1\Gamma_2 g_1^2 g_2^2 ,\\
B &= 2\Gamma_{21} g_1^2 g_2^2 (\Gamma_1 g_1^2 + \Gamma_2 g_2^2 + 4\Gamma_{21}\Gamma_1\Gamma_2) ,\\
C &= 16\gamma_1\Gamma_2 g_2^2 ,\\
D &= 4\big\{ -2\gamma_1\Gamma_2 g_2^4 + 4\Gamma_1\Gamma_2(\gamma_2\Gamma_2 g_1^2 + \gamma_1\Gamma_1 g_2^2)\\
&\quad + 4\Gamma_{21}^2\gamma_1\Gamma_2 g_2^2 + [\Gamma_{21}\gamma_1 - \Gamma_2(\gamma_1+\gamma_2-6\Gamma_1)] g_1^2 g_2^2 \big\} ,\\
E &= 16(\gamma_2\Gamma_1 g_1^2 + \gamma_1\Gamma_2 g_2^2) ,\\
F &= 4\big\{ 2\gamma_1\Gamma_2 g_2^4 - 2\gamma_2\Gamma_1 g_1^4 - 8\Gamma_{21}^2\gamma_1\Gamma_2 g_2^2\\
&\quad + g_1^2 g_2^2 [(\gamma_1+\gamma_2)(\Gamma_2-\Gamma_1) - \Gamma_{21}(3\gamma_1+\gamma_2)] \big\} ,\\
G &= 8\Gamma_{21}\big[2\Gamma_{21}(\gamma_2\Gamma_1 g_1^2 + \gamma_1\Gamma_2 g_2^2) + (\gamma_1+\gamma_2) g_1^2 g_2^2 \big] ,\\
H &= (\Gamma_1 g_1^2 + \Gamma_2 g_2^2 + 4\Gamma_{21}\Gamma_1\Gamma_2) \times \big[(\gamma_1+\gamma_2+6\Gamma_{21}) g_1^2 g_2^2\\
&\quad + \gamma_2 g_1^4 + \gamma_1 g_2^4 + 4\Gamma_{21}(\gamma_2\Gamma_2 g_1^2 + \gamma_1\Gamma_1 g_2^2) \big] .
\end{aligned}
$$

Here γ_1 and γ_2 are the population decay rates from the excited state into ground states $|1\rangle$ and $|2\rangle$, Γ_1 and Γ_2 the corresponding dephasing rates, and Γ_{12} the dephasing of the ground state coherence. n_3 is proportional to the absorption coefficient for the combined laser beams [14]. The only approximation that was used for the derivation of (14) is that direct population transfer between the two ground states is neglected (inclusion of this process makes the resulting formulae *much* more complicated).

Figure 2 shows an example for the shape of the dark resonance on the D_2 line in cesium vapor at room temperature, measured both in absorption and dispersion [15]. Here ω_2 was held constant at $\omega_2 = \omega_{32}$ and ω_1 was scanned around ω_{31}. As long as ω_1 is detuned from ω_{31} light field 2 optically pumps the population into state $|1\rangle$. When light field 1 becomes resonant it therefore experiences increased absorption. However, when both fields are fully resonant with their respective optical transitions and one would naively expect maximum absorption a narrow dip is seen: the coherent population trapping cancels the absorption. The overall absorption curve looks approximately like a Lorentzian with the width of the homogeneously broadened optical transition and a much narrower inverted Lorentzian at the center. Correspondingly, the index of refraction is the superposition of a dispersive Lorentzian with anomalous dispersion near $\delta_R = 0$ and a narrow dispersive Lorentzian of opposite sign, i.e., with normal dispersion at $\delta_R = 0$. This behavior follows the theoretical prediction [16].

What makes coherent population trapping resonances so interesting for precision applications is the small linewidth of the dark resonance. The relevant parameter is the lifetime of the ground state coherence responsible for the trapping effect. Since $|1\rangle$ and $|2\rangle$ have equal parity the dominant radiative decay process is the magnetic dipole transition connecting $|1\rangle$ and $|2\rangle$ with a spontaneous lifetime of several thousand years. This is clearly negligible so that experimental parameters determine the observed linewidth: the stability of $\Delta\omega$ and $\Delta\varphi$, Doppler broadening, power broadening, collisions, and external fields. In multilevel atoms the coherence can also be destroyed by optical excitation into additional excited states through one-photon absorption. Furthermore, higher-order processes, for example, four-photon processes, can give a small contribution under special circumstances [17]. Some of the broadening mechanisms also cause shifts of the resonance frequency, with important consequences for the accuracy of precision experiments.

The characteristics of coherent population trapping resonances are determined by the behavior of the ground state hyperfine coherence induced in the presence of the two light fields. Such coherences have long been studied in radio frequency (rf) spectroscopy and it is expected that the basic physics of coherent population trapping resonances and of rf resonances are the same. For instance, this is true for various relaxation cross sections and systematic effects, as will be shown in later parts of this work. There are, however, some differences (Fig. 3). Because two photons are used to couple the two ground states at a dark resonance it is possible to induce $\Delta m = 0, \pm 1, \pm 2$ coherences as opposed to standard (one-photon) rf excitation where only $\Delta m = 0, \pm 1$ is possible. This becomes apparent, for example, when a small magnetic field lifts the degeneracy of the lower magnetic sublevels.

A distinct advantage of the optical dark resonances compared to radio frequency excitation is that glass fibers can be used to transport the excitation radiation to the sample. This is especially beneficial for sensitive magnetometers because all magnetic and electric components can be kept away from the measurement volume. Furthermore, in principle a spatial resolution in the micrometer range is possible with optical excitation, as opposed to cm-sized excitation regions in rf experiments.

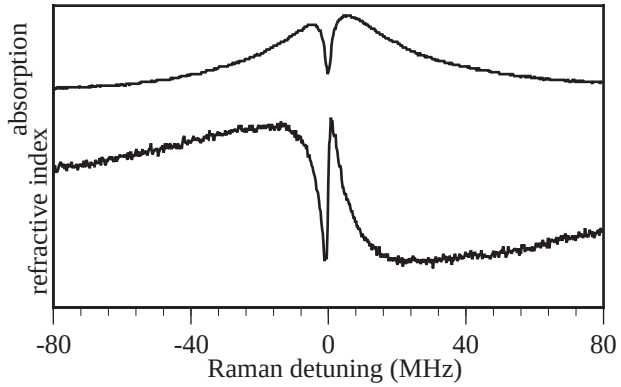

Fig. 2. Low-resolution absorption and dispersion spectra measured in the vicinity of the coherent population trapping resonance as a function of Raman detuning δ_R

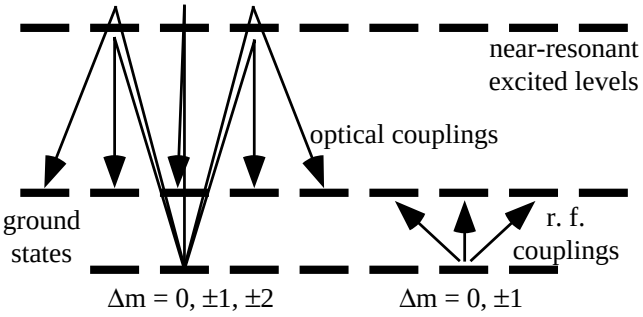

Fig. 3. Similarities and differences between coherent population trapping resonances and rf resonances

2 Optical phase-locking

2.1 Light sources: diode lasers

All experiments described in the following chapters were performed near 850 nm wavelength. In this spectral region AlGaAs semiconductor diode lasers are the most convenient source of narrow-band radiation: they are small, affordable, and their spectral characteristics can easily be adjusted by a variety of techniques, among them optical and electrical feedback. The operation of diode lasers for precision spectroscopy has been perfected over the last few years, and we have developed and optimized a robust and versatile design. The basic concepts are similar to those published in two review articles [18, 19].

The setup consists of a commercial laser diode (including the glass window of the SOT-148 package) with feedback from a holographic diffraction grating in Littrow configuration. The spectral characteristics of these laser sources are of particular interest. While the linewidth for short averaging times (< ms) is less than 1 MHz, acoustic and thermal fluctuations cause jumps and drifts of this narrow line in a region of a few MHz width. In order to eliminate these slow effects it is standard routine to lock the laser frequency with a relatively slow servo loop to a stable reference, here usually a Doppler-broadened absorption line of cesium vapor. If necessary, the laser can also be stabilized to Doppler-free saturated absorption lines [20] which increases the reproducibility of the central frequency because of the narrower spectral features (10 MHz width as opposed to 400 MHz for a Doppler-broadened absorption line).

2.2 A brief overview of modulation techniques

In order to achieve narrow linewidths for precision measurements the coherent population trapping resonances have to be excited by two light fields that are coherently coupled. The general definition of coherent coupling of light fields demands a fixed phase relation between the two fields. For example, in order for the two fields

$$E_1 = E_{01}\cos(\omega_1 t + \varphi_1(t))\,, \tag{15}$$

$$E_2 = E_{02}\cos(\omega_2 t + \varphi_2(t)) \tag{16}$$

to be coherently coupled, $\varphi_1(t) - \varphi_2(t)$ has to be constant. Note that the frequencies ω_1 and ω_2 do not have to be equal but that the instantaneous frequency difference,

$$\Delta\omega = \frac{\mathrm{d}}{\mathrm{d}t}\big(\omega_1 t + \varphi_1(t) - \omega_2 t - \varphi_2(t)\big) = \omega_1 - \omega_2\,, \tag{17}$$

is fixed in time. The stabilization of the relative phase of two light fields is therefore a convenient way of keeping the difference frequency of the two optical oscillators strictly constant.

A rather straightforward way to obtain coherently coupled light fields is to modulate a laser beam and to exploit the fixed phase relationship between the carrier and the modulation sidebands. Several modulation techniques are possible in principle: acoustooptic modulation (AOM), electrooptic modulation (EOM), and direct laser current modulation. For experiments on sodium, where the ground state splitting is only 1.77 GHz, the AOM technique is the method of choice, such as, for instance, for the construction of an atomic beam frequency standard [3]. It is completely impractical to use AOMs at the long wavelength (850 nm) and high modulation frequency (9.2 GHz) required for cesium vapor. The high modulation frequency poses a problem even for EOMs because they require a traveling-wave design with matched phase velocities for the laser light and the modulating radio frequency field. Modulation frequencies of 88 GHz and more have been achieved in special designs [21, 22], and for 9.2 GHz there is even a commercial model (NewFocus 4851) using a tuned rf resonator with high driving power. However, as will be shown in Sect. 5.2.2, even small changes in the light intensities cause a frequency shift [14] of the coherent population trapping resonances. It is therefore extremely important to have constant modulation efficiency, which can only be obtained with a thermal stabilization of the EOM and its rf resonator to within about a millikelvin. Because at the same time several watts of rf power are sent into the device, electrooptic modulation is not feasible here either.

A very attractive option is the direct modulation of the laser diode injection current. Efficient modulation is possible up to the relaxation oscillation frequency of the laser medium, typically 1–3 GHz in edge-emitting semiconductor lasers. At higher frequencies the intrinsic modulation efficiency drops dramatically, an effect that is made even worse by the low feed-through efficiency of the standard SOT-148 package of the laser chip.

There have been reports on a cesium magnetooptical trapping experiment [23] and on coherent population trapping in a cesium beam [24] where a commercial laser diode was modulated at 4.6 GHz using high rf power so that the first upper and lower sidebands were driving the two hyperfine components of the D_2 line. For coherent population trapping experiments using vapor cells containing an additional buffer gas this approach has the disadvantage that the pressure-broadened optical transition would also be more or less resonant with the strong carrier wave and therefore lead to a destruction of the coherent dark state through one-photon excitation. One could overcome this limitation by spatially separating the carrier from the sidebands but in general complicated and delicate experimental setups are required.

In our experiments we have not been able to achieve a significant modulation index by 9.2 GHz current modulation of a packaged commercial diode laser. There are, however, new perspectives for the near future because recently vertical cavity surface emitting lasers (VCSELs) were demonstrated at wavelengths near the cesium and rubidium lines with a 3 dB modulation bandwidth of more than 10 GHz [25]. Very recently we have obtained first results with such a prototype VCSEL. It is envisioned that a directly modulated VCSEL could eventually become the system of choice for the observation and application of coherent population trapping in cesium or rubidium vapor.

2.3 Optical phase-locking

The most versatile strategy for the coherent coupling of light fields is the use of optical phase-locked loops where an electronic servo loop controls the optical phase of a laser light beam (“slave”) relative to that of a reference laser (“master”). In principle arbitrarily high difference frequencies are

possible using nonlinear optical techniques. Hundreds of terahertz have been used in optical frequency metrology [26, 27]. The two phase-locked light beams are geometrically completely independent so that both can have any direction, diameter, polarization, and power, as opposed to all other methods. Optical phase-locking, first demonstrated in 1965 [28], has been studied for applications in communications [29] and phased-array laser radar [30] and perfected for pulse synthesis [31, 32] and optical frequency multiplication chains [33, 34].

The setup of the optical phase-locked loop employed in this work is sketched in Fig. 4. The light beams from master and slave laser are mode-matched and superposed on a photodiode (Antel Optronics AR-S2) that is fast enough to detect the 9.2 GHz beat signal S_{beat} required for the cesium vapor experiments:

$$S_{\text{beat}} = \left\langle |E_{\text{slave}} + E_{\text{master}}|^2 \right\rangle_t \tag{18}$$

$$= \Big\langle \big| E_{01}\cos(\omega_1 t + \varphi_1(t)) + E_{02}\cos(\omega_2 t + \varphi_2(t)) \big|^2 \Big\rangle_t \tag{19}$$

$$= E_{01}E_{02}\cos(\Delta\omega t + \Delta\varphi(t)) + \text{dc terms} \tag{20}$$

with $\Delta\omega = \omega_1 - \omega_2$ and $\Delta\varphi = \varphi_1 - \varphi_2$. After amplification the beat signal is compared with a rf signal from a local oscillator at the desired difference frequency $\Delta\omega/2\pi$ in a two-step process. In a double-balanced mixer the beat signal is down-converted into the 20 MHz range where a digital phase/frequency detector gives an output signal proportional to the phase difference between $\Delta\varphi$ and the local oscillator phases $\varphi_{\text{LO1}} + \varphi_{\text{LO2}}$.

The design of this phase detector follows an idea by Hall et al. [35] and its implementation is similar to that described by Prevedelli et al. [34]: one of the input signals is fed to an upward counting 5-bit TTL counter while the other one is connected to a downward counter. When both lasers are phase-stable the 5-bit sum of the two counters remains basically constant and its time-average is proportional to the phase difference. In this way phase excursions $\Delta\varphi$ of $\pm 32\pi$ around the reference phase can be detected, which makes the servo loop robust enough to phase-lock two grating-stabilized lasers for many hours even in a noisy laboratory environment. Additionally, logic gates switch the detection mode to frequency detection when large phase excursions cause an overflow of the adder. During this time the coherent coupling between the two light fields is lost but the frequency detection mode helps to pull the slave laser frequency back into the range where the phase-locked loop can recapture it.

The servo loop is closed by a passive loop filter tailored to compensate part of the electronic phase delay accumulated along the servo loop. The filtered servo signal is directly coupled to the pins of the laser's SOT-148 package in order to have good high-frequency response. Low-frequency drifts are eliminated by electronically integrating the error signal and adding it to the offset voltage of the grating piezo element. Loop bandwidths in excess of 2 MHz can be obtained, and within the servo bandwidth the optical phase of the slave laser follows the master laser phase typically within $\Delta\varphi_{\text{rms}} = 4°$.

The coherent coupling can routinely be maintained for hours, and both large and small difference frequencies are possible. Note also that offset voltages in the servo amplifiers may cause constant phase offsets but no frequency offsets since frequency is the derivative of phase. This particular practical advantage has been used in experiments designed to check the accuracy of the 1:2 frequency ratio between fundamental and optical second harmonic [36], of the frequency accuracy of a degenerate optical parametric oscillator [37], and of an optical frequency comb generator [38].

Finally, two important points about the requirements for an optical phase-locked loop should be mentioned. In the presence of external noise the residual instantaneous frequency difference

$$\Delta\omega(t) = \frac{\mathrm{d}}{\mathrm{d}t}\big(\Phi_1(t) - \Phi_2(t)\big), \tag{21}$$

where $\Phi_1(t)$ and $\Phi_2(t)$ are the total accumulated phases of master and slave, is not constant but fluctuates around a mean value $\omega_1 - \omega_2$. The maximum phase excursion that can still be followed is limited by the detection range of the phase detector. While the simplest phase detectors for phase-locked loops allow no more than $\pm\pi$ excursion the detector used here has a phase error range of $\pm 32\pi$ which makes it much more robust. Furthermore it is important how quickly $\Phi_1(t) - \Phi_2(t)$ fluctuates. In a frequency chain for metrological applications [27] this parameter is uncritical because only the total number of optical cycles during the averaging time of typically 1 s per data point is important. In the experiments on coherent population trapping, however, phase excursions of more than $\pi/2$ during the lifetime of the ground state coherence, typically milliseconds, would lead to a destruction of the coherence and a broadening of the resonance line.

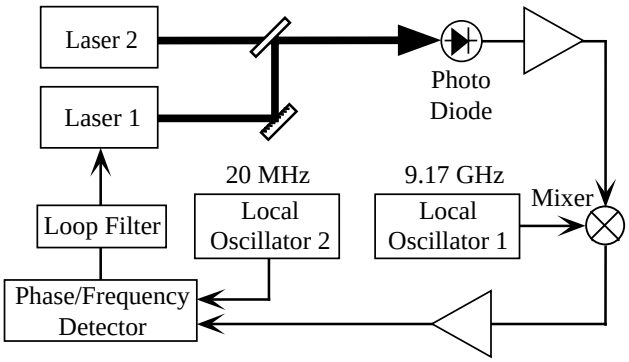

Fig. 4. Setup for optical phase-locking at large difference frequency

3 Experimental test of the three-level theory

3.1 Atomic properties of cesium

The cesium atom is very convenient for laser spectroscopy because its D_1 and D_2 resonance lines are accessible by diode lasers and because at room temperature its vapor pressure of about 1.6×10^{-4} Pa is sufficient for spectroscopic experiments. Most measurements discussed in the following sections were performed with grating-stabilized diode lasers (a few older experiments used diode lasers stabilized to external high-finesse Fabry–Pérot cavities by resonant optical feedback, "Hollberg" design [39–41]).

The cesium D_2 line only provides an approximation to an ideal three-level system (Fig. 5). In zero magnetic field the $^6S_{1/2}$ ground states with $F = 3$ and $F = 4$ can be identified with $|1\rangle$ and $|2\rangle$ in Fig. 1 while the one-photon electric dipole selection rules allow both $^6P_{3/2},\ F = 3$ and $^6P_{3/2},\ F = 4$ to play the role of the excited state $|3\rangle$. In a magnetic field the degeneracy of the Zeeman levels is lifted, and each state splits into $2F + 1$ components with a Zeeman shift as given in Fig. 5.

In a thermal vapor all the optical transitions are Doppler broadened to about 370 MHz so that the upper levels overlap while the ground states are still completely separated. For each optical detuning δ there are two velocity groups of cesium atoms (labeled "v_3" and "v_4") that can form Λ systems: group "v_3" is resonant with the transitions to $|\,^6P_{3/2},\ F = 3\rangle$, and group "$v_4$" forms a Λ system with $|\,^6P_{3/2},\ F = 4\rangle$. As will be shown in Sect. 4.3 one can treat the resulting dark resonance spectra as if for each atom the light fields interacted with *either* the upper $F = 3$ *or* the upper $F = 4$ level. The dark resonance spectrum is therefore the sum of two spectra, one for $|3\rangle = |\,^6P_{3/2},\ F = 3\rangle$ and another one for $|3\rangle = |\,^6P_{3/2},\ F = 4\rangle$, each weighted with the number of atoms in the corresponding velocity group according to the Maxwell distribution.

The D_2 line is not ideally suited for experiments on coherent population trapping because due to the Doppler broadening the excited $F = 2$ and $F = 5$ levels can be populated by off-resonant one-photon absorption from the ground state $F = 3$ and $F = 4$ levels, respectively. These loss channels for the ground state coherence give an additional small contribution to the width of the dark resonance line and – more importantly – provide background absorption. Therefore 100% transparency cannot be reached using the D_2 line in a vapor. This should be different on the D_1 line at $\lambda = 894$ nm (where diode lasers are harder to obtain and were not available for the experiments described in this work). Atomic beam experiments can also avoid this loss channel; 90% reduction of fluorescence has been seen in a sodium beam experiment [42].

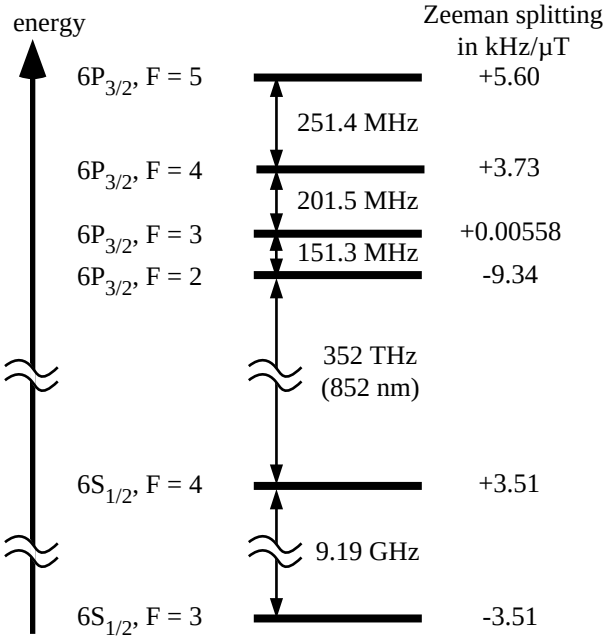

Fig. 5. Participating energy levels in the cesium D_2 line (not to scale)

3.2 Experimental setup

The core of the experimental setup are two grating-stabilized diode lasers phase-locked to each other at 9.2 GHz difference frequency (Fig. 6). A small part of the power from the lasers is superposed on a fast photodiode for the optical phase-locked loop. The first local oscillator is a low phase noise dielectric resonance oscillator at 9.172 GHz injection-locked by the 183rd subharmonic at 50.12367 MHz provided by a stable radio frequency synthesizer. A second synthesizer, stabilized to the same 10 MHz reference oscillator as the first one, provides a computer-tunable 20 MHz signal as the second local oscillator frequency. In a typical experiment laser frequency ω_2 is locked to the $F = 3, 4$ crossover transition of the saturated absorption spectrum [20] in an auxiliary cesium vapor cell while laser frequency ω_1 is scanned across the Raman resonance by detuning local oscillator 2.

Since the residual Doppler effect would broaden the dark resonance line to 300 kHz even when the two light beams make an angle of only 0.5 mrad with each other [43, 44] the major part of the laser powers is coupled into a stretch of single-mode optical fiber. At the fiber output both beams overlap perfectly in a clean circular Gaussian mode.

The laser beams are polarized and sent through a glass cell containing the cesium vapor. The cell is surrounded by three mutually perpendicular pairs of current-carrying coils that compensate static magnetic fields such as the geomagnetic field. By changing these currents small magnetic fields can be applied in any direction.

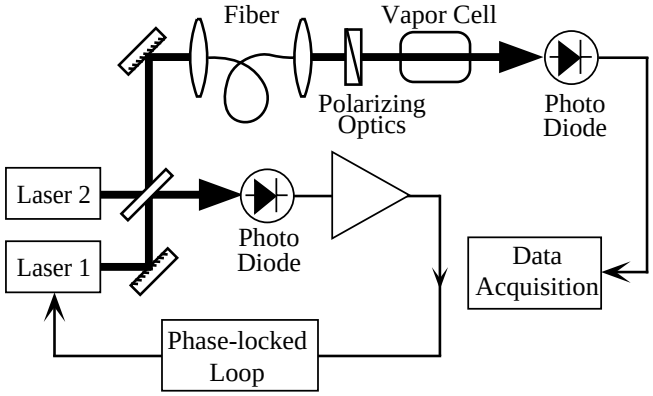

Fig. 6. Experimental setup for the observation of coherent population trapping resonances in a cesium vapor cell

3.3 Observation of dark resonances in pure cesium vapor

Usually the signal transmitted through the atomic vapor is recorded. Alternatively the spatial distribution of the fluorescence intensity of the cesium vapor can be recorded with a CCD camera (Fig. 7a). The intensity decreases towards the end of the cell because part of the laser power has already been absorbed in the preceding stretch of the cell. When $\Delta\omega$ is tuned to the coherent population trapping resonance

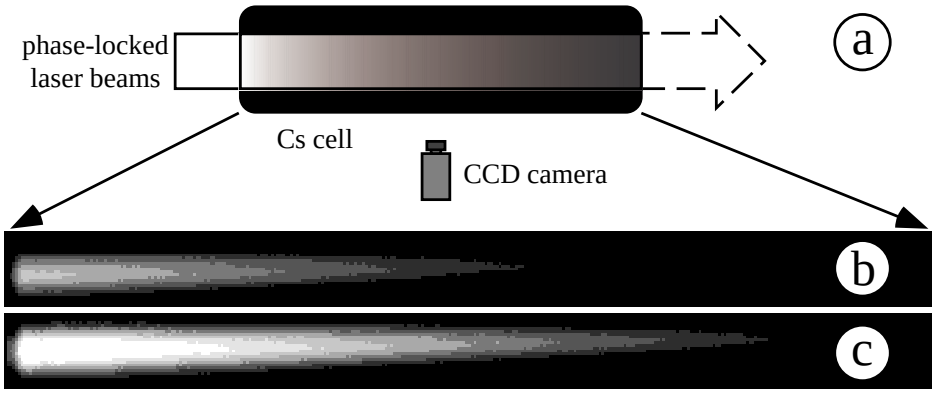

Fig. 7. Grayscale images of the spatial distribution of fluorescence from a cesium vapor cell of length 7 cm in the presence of a bichromatic light field.**a** Experimental setup. **b** Laser difference-frequency tuned to the 9.2 GHz hyperfine splitting: the dark resonance. **c** Small Raman detuning: a bright resonance. Absorption along the cell reduces the fluorescence intensity towards the end of the cell

(Fig. 7b) the cell becomes darker (hence a "dark" resonance) than for a small Raman detuning (Fig. 7c).

The dark resonance has the interesting property that there is a steep dispersion at the resonance center where the absorption vanishes (Fig. 2). This is in contrast to the behavior of a bright resonance where at the point of steepest dispersion the absorption has a maximum. In order to measure the dispersion near the dark resonance simultaneously with the absorption the vapor cell was placed inside a Mach–Zehnder interferometer where laser 1 has equal power in both interferometer arms [15, 44]. Along one arm the light from laser 2 is superposed. Both arms meet on a beamsplitter with exactly 50% splitting ratio. The difference of the signals from the two interferometer output ports was held constant by changing one arm length via a mirror mounted on a piezo element. The piezo voltage is then proportional to the nonlinear index of refraction n_{nl} so that undistorted spectra of n_{nl} can be obtained [15] (Fig. 2). This is in contrast to an experiment on a dark resonance in a cascade-type level scheme ($\Omega_2 > \Omega_3$ in Fig. 1) in rubidium vapor [45].

Experimentally one finds that on resonance the nonlinear part of the absorption coefficient is almost zero while the change of refractive index is – to our best knowledge – the strongest ever measured [15]. While n_{nl} is very small, its frequency dependence is dramatic: $\mathrm{d}n/\mathrm{d}f = 1.1 \times 10^{-11}$ /Hz (for comparison, BK7 glass in the near infrared has $\mathrm{d}n/\mathrm{d}f = 4.4 \times 10^{-17}$ /Hz). Since the density of cesium vapor at room temperature is 10^{11} times lower than that of glass the dispersion per atom is more than 10^{16} times higher in the dilute vapor than in the glass.

A different measure for the steepness of the dispersion is the group velocity $v_{\mathrm{g}} = \mathrm{d}\omega/\mathrm{d}k$ or the group index $n_{\mathrm{g}} = c/v_{\mathrm{g}} = n + \omega \times \mathrm{d}n/\mathrm{d}\omega$. For example, Schmidt et al. found a maximum value of $n_{\mathrm{g}} = 3400$ at the center of the resonance in a room-temperature cell [15]. The group index goes through a maximum as a function of laser intensity. Heating the cell increases the vapor density, and $n_{\mathrm{g}} = c/10000$ was easily obtained in this way.

These values of n_{g} have to be compared with $n_{\mathrm{g}} = 14$ found in the vicinity of a conventional one-photon resonance in rubidium vapor [46], $n_{\mathrm{g}} = 1000$ for the special pulses in self-induced transparency [47], $n_{\mathrm{g}} = 13.2$ for the dispersion in the rubidium ladder system [45], and $n_{\mathrm{g}} = 165$ at a dark resonance in lead vapor [48]. Group velocities of $c/10\,000$, as obtained here, are less than a factor of 10 higher than the speed of sound in solids – "slow" light indeed!

3.4 Effects of an additional buffer gas

The narrowest dark resonance lines that could be obtained in cesium vapor cells have a full width at half maximum (FWHM) of about 10 kHz, limited by the short interaction time of 35 μs for atoms with thermal velocity and a laser beam diameter of 0.7 cm [6]. In order to narrow the resonance lines even further the effective interaction time between atoms and light has to be increased.

Using Ramsey excitation of a sodium atomic beam with a zone separation of 30 cm a Ramsey fringe of 1.3 kHz linewidth was observed by Thomas et al. [49]. Further reduction by almost two orders of magnitude is possible using improved vapor cells. One possibility is to coat the cell walls with a suitable substance, for example, paraffin [50] or organosilanes [51]. Alkali atoms bounce off these films with very small sticking probability so that the ground state coherence survives hundreds or thousands of wall collisions, thus effectively increasing the interaction time by a large factor.

Another approach is the use of "buffered" cells: an inert gas, neon for instance, at pressures of several kPa is added to the cesium vapor. Frequent collisions with neon atoms impede the free motion of cesium atoms through the light beam so that transit times of many milliseconds are possible. Since the ground state coherence has magnetic dipole character millions of collisions with neon atoms (no net spin, very small polarizability) are necessary to destroy it. The optical transitions, in contrast, are strongly broadened by buffer gas collisions to several 100 MHz already for a few kPa of neon. Fine-structure changing collisions, i.e., an exchange of population between the $^6P_{1/2}$ and $^6P_{3/2}$ levels, are completely negligible for cesium in neon [50].

Buffered cells have been used in optical pumping experiments in rf spectroscopy since the mid-fifties. There is a large body of literature on the effects of wall coatings, buffer gases, and their combination on rf and optical transitions. Because of the similarity between the physics underlying rf and population trapping experiments one can expect these findings to be transferable to coherent population trapping. In the comprehensive review by Happer [50] several hundred references to theoretical and experimental work on relaxation processes and cross sections are given together with tables of experimentally determined values. It is therefore surprising that no systematic studies of buffer gas effects on coherent population trapping existed. The only exceptions are a plot of the dark resonance linewidth and contrast in sodium vapor

as a function of helium pressure [52], a similar but uncommented curve in [53] and a plot of the dark resonance line shape for sodium in helium in [54].

Because of the broad homogeneous linewidth the contrast of coherent population trapping resonances is lower in buffered cells so that frequency modulation (FM) spectroscopy is used to measure the transmission spectra. For that purpose the frequency of local oscillator 2 (cf. Fig. 4) is modulated with typically 1 kHz frequency and 1 kHz amplitude. Profiles of resonance lines broader than 1 kHz look basically like the derivative of the underlying absorption line profile, whereas for narrower lines the profiles are more complex [55]. With a simple numerical procedure even the line shapes in the most general case can be inverted, and both the absorption and the dispersion line shapes can be calculated from a single transmission measurement using the in-phase and quadrature components of the FM signal [56, 57]. However, the modulation frequency must be a multiple of the frequency step size in order for the method to work so that most of the spectra taken before the development of the inversion procedure had to be analyzed by fitting position, height, and width of the calculated FM signals to the experimental spectra, assuming Lorentzian absorption and dispersion profiles for the dark resonances.

In order to observe the effect of the buffer gas more clearly the vapor cell was placed in a small longitudinal magnetic field ($B = 24\,\mu$T). The ground and excited states are split by the Zeeman effect, and for equal circular laser polarizations the dark resonance splits into seven components at different resonance frequencies. The details of the behavior of the dark resonance in magnetic fields will be discussed in the following section. Here it is sufficient to know that there is a component (corresponding to the coupling of $|F = 3,\ m_F = 0\rangle$ and $|F = 4,\ m_F = 0\rangle$, the so-called 0-0 component) that remains at the original resonance frequency because in first order it is not shifted by the magnetic field. Its width is not influenced by field inhomogeneities and therefore it was chosen for further detailed studies.

A special cesium vapor cell was used that could repeatedly be filled with different buffer gas pressures using a glass valve. For each neon pressure a series of measurements for different laser intensities and magnetic fields were taken and fitted with the theoretical line shape in order to obtain the values for height, width, and position of the resonance. In Fig. 8 the full width at half maximum (FWHM) of the coherent population trapping resonance is plotted versus neon pressure. For increasing pressure a dramatic decrease due to longer interaction time is followed by a slow increase due to collisional broadening. There is a broad plateau where the FWHM is below 100 Hz. The narrowest resonance line observed has a FWHM of 42 Hz and is shown as an example in Fig. 9. The broader pedestal is due to residual line frequency interference into the phase-locked loop.

The solid line in Fig. 8 is a calculation taking into account diffusion (γ_{diff}) of cesium atoms in neon and collisional relaxation (γ_{coll}):

$$\text{FWHM} = \frac{1}{\pi}\,(\gamma_{\text{diff}} + \gamma_{\text{coll}}) \tag{22}$$

$$= 1.3 \times 10^5 \frac{\text{Pa}}{\text{s}} \frac{1}{p} + 4 \times 10^{-3} \frac{p}{\text{s Pa}}\,. \tag{23}$$

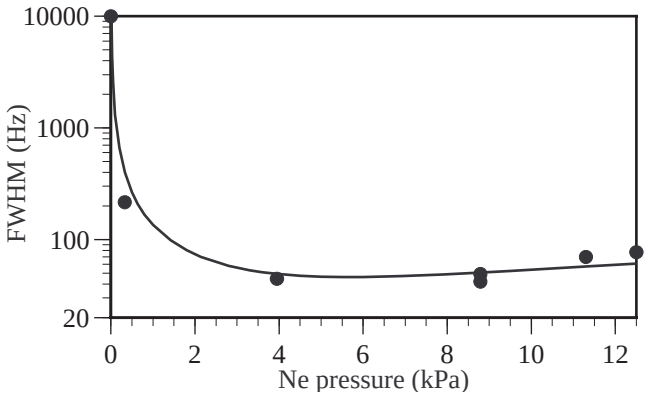

Fig. 8. Full width at half maximum (FWHM) of coherent population trapping resonances in cesium vapor as a function of neon buffer gas pressure. The *solid line* is calculated without any free parameters

The numerical values were computed using the cross section and diffusion data determined by Beverini et al. [58] in an optical pumping experiment. The good agreement with the experimental points is a further indication that the optical phase-locked loop really eliminates all difference frequency fluctuations as expected.

The data of Fig. 8 were taken with laser intensities around $0.01\,\text{mW/cm}^2$. For higher intensities power broadening sets in (Fig. 10). A linear relation between FWHM and g_Λ^2 is expected [12, 59]:

$$\text{FWHM} = 2\Gamma_{12} + g_\Lambda^2/(\gamma_1 + \gamma_2)\,, \tag{24}$$

if the intensity is below the coherence saturation intensity

$$I_{\text{c}} = 4\pi hc\Gamma_{12}/3\lambda^3\,. \tag{25}$$

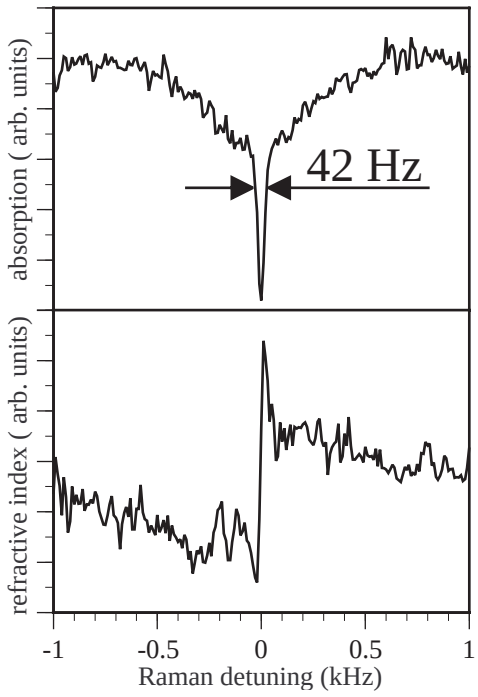

Fig. 9. Absorption and dispersion spectrum of a very narrow *dark resonance line*, obtained by numerical inversion of the FM line shape

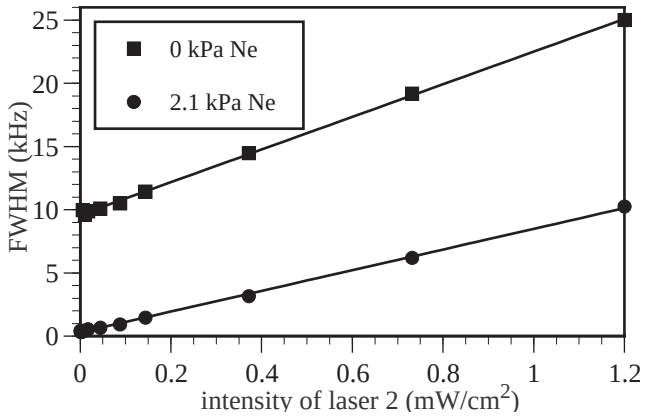

Fig. 10. Power broadening of the 0-0 component with and without buffer gas

Using the axis offset value of the linear fit curves to the data in Fig. 10 as an upper limit for Γ_{12} one obtains $I_c = 8.0 \times 10^{-3}\,\mathrm{mW/cm^2}$ and $I_c = 2.5 \times 10^{-4}\,\mathrm{mW/cm^2}$ for 0 and 2.1 kPa neon, respectively. So the coherence saturation intensity is much smaller than the smallest laser intensity for which the dark resonance spectrum can be measured with sufficient signal-to-noise ratio. Experimentally one still finds a linear relationship with a slope of about $10\,\mathrm{kHz/(mW/cm^2)}$ which is a factor of 200 lower than predicted from (24) for $I < I_c$. Such a decrease in slope has also been seen – although much less dramatic – by Akulshin et al. [43, 59]; they were able to measure the dark resonance width both above and below I_c because due to the instability of the laser difference frequency in their setup the relaxation rate of the ground state coherence (and therefore I_c) was a hundred times larger than it is here.

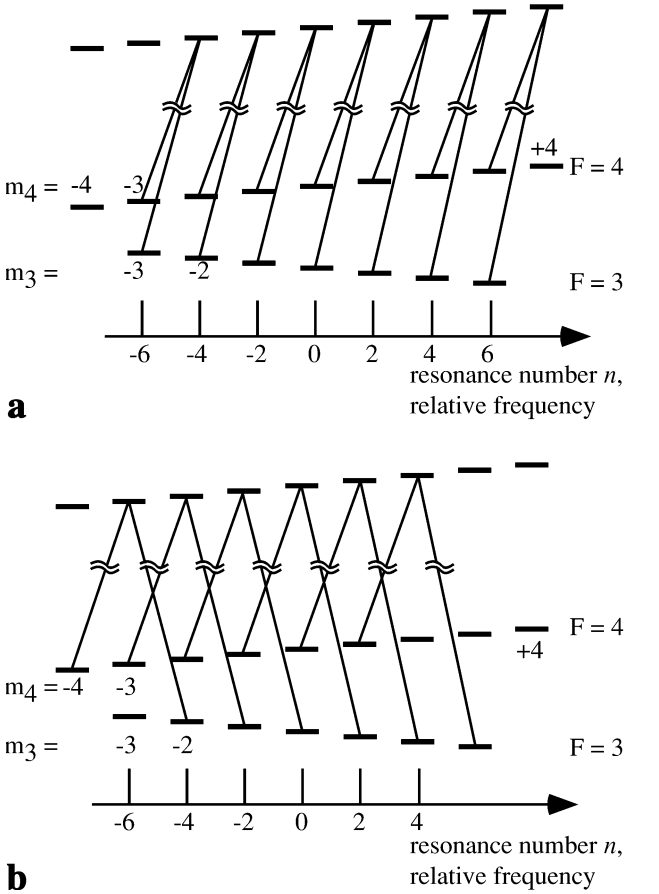

Fig. 11a,b. Zeeman-split cesium dark resonances in a longitudinal field with **a** $\sigma^+\sigma^+$, **b** $\sigma^+\sigma^-$ excitation. The selection rules allow seven (or six) Λ resonances, with frequency positions indicated by the short vertical lines. Possible couplings between pairs of ground state levels are indicated schematically by diagonal lines

4 Multilevel theory

In order to use coherent population trapping resonances for precision measurements of magnetic fields it is essential to have a detailed understanding of their behavior in magnetic fields. This includes selection rules, positions, and relative strengths of all Zeeman components.

For the relatively small flux densities B considered here the complete Breit–Rabi formula for the energy levels as a function of magnetic field reduces to the linear Zeeman case where the magnetic substates are Zeeman-shifted at a rate of $-\xi B m_3$ and $+\xi B m_4$, respectively, with $\xi = g_J \mu_B/(2I+1)h = 3.5\,\mathrm{kHz}/\mu\mathrm{T}$. g_J is the electronic g-factor and μ_B the Bohr magneton while m_3, m_4 are the magnetic quantum numbers in the $F = 3$ and $F = 4$ ground states. Hence instead of just two lower states there are $4I + 2$ (I is the nuclear spin quantum number, $I = 7/2$ in cesium), allowing the formation of several Λ systems, depending on field direction and laser polarizations. Two examples are shown schematically in Fig. 11. Each component is offset in frequency by $f_n = n\xi B$, where $n = m_3 + m_4$.

It is not immediately obvious how to extend the simple Λ system picture to this multilevel system in the general case. In the following, symmetry arguments are used to calculate the selection rules and relative line strengths in a superposition of Λ systems in alkali atom ground states, both with and without the presence of a buffer gas. In Sect. 4.3 the results will be compared to experiments on the D_2 line in cesium vapor. This section basically covers the work described in more detail in [60].

4.1 Theoretical model

For a complete description of the behavior of the atom in the presence of the two light fields the equations of motion for the density matrix have to be solved. This is a rather cumbersome calculation because of the large number of levels involved (48 levels for the D_2 line of cesium). Many authors have solved this problem numerically (see Arimondo's review article [12] for references). The numerical solution, however, makes it hard to obtain physical insight. On the analytical side, there is a series of papers by a theoretical group in Novosibirsk that culminated in [61] where for zero magnetic field the density matrix was expanded into a series of invariant parts, valid in the case of purely radiative damping. Hioe and Carroll [62] found general invariants in multilevel quantum systems, while Kanokogi and Sakurai [63] gave another elegant approach which, however, takes only one excited level into account.

The key idea of our own model is to separately consider all possible "Zeeman-Λ systems", i.e., Λ systems involving

pairs of magnetic substates with one state taken from each ground state F level. Here the states $\{|\psi\, F\, m_F\rangle\}$ are a suitable basis where $|\psi\rangle$ is a shorthand notation for $|\nu\, L\, S\, J\,\rangle$ (ν is the principal quantum number while L, S, and J are those of the orbital, spin, and total electronic angular momentum). The ground state sublevels and the bichromatic light field are mainly characterized by their respective angular momenta. Hence the elegant formalism of tensor algebra can be used in order to derive geometry-dependent selection rules and coupling strengths.

However, in order for the reduction to tensor algebra to be valid, several simplifying assumptions have to be made:

No Zeeman optical pumping. The overall shape of a dark resonance spectrum in a magnetic field can be influenced by optical pumping. But for sufficiently low laser power or high buffer gas pressure optical pumping can be neglected, as shown in [60].

No one-photon absorption. In the case of alkali D_2 lines the excited states $F = I \pm 3/2$ cannot couple to *both* ground states simultaneously. These levels therefore form a loss channel for the coherent state through one-photon absorption. In general the one-photon transition rates are different for different coherent states and can change the population balance between the coherent dark states. This one-photon loss mechanism is ignored here.

No multilevel coherences. Depending on the experimental parameters some sublevels of the ground state can simultaneously be coupled to more than one other ground state sublevel. In this simple model all interference effects (i.e., coherences involving more than two photons) due to shared levels among pairs of ground states are ignored. The comparison with experimental results shows that this approach is, indeed, justified.

Under these assumptions it is reasonable to assume that the total line strength of the resonance is distributed among the Zeeman-Λ systems according to their relative strengths. Since in the unsaturated case the contrast of the Λ resonance line increases with laser intensity [12], i.e., Rabi frequency, the relative strength of a Zeeman-Λ system is given by the two-photon coupling strength between the pair of ground states involved. In the frame of the model this coupling strength is obtained for each pair $\{|\psi_i\, F_i\, m_i\rangle, |\psi_f\, F_f\, m_f\rangle\} = \{|i\rangle, |f\rangle\}$ by calculating the matrix element of an effective two-photon operator $\mathcal{O}_\Lambda$ for the transition from $|i\rangle$ to $|f\rangle$. This includes a summation over all possible upper states and all polarization components present in the light fields:

$$S_{\mathrm{rel}}(m_i, m_f) = |A_\Lambda(m_i, m_f)|^2 \tag{26}$$

$$\propto |\,\langle\psi_f\, F_f\, m_f|\,\mathcal{O}_\Lambda\,|\psi_i\, F_i\, m_i\rangle\,|^2\,. \tag{27}$$

The effective two-photon operator $\mathcal{O}_\Lambda$ describes a process where one photon is absorbed from one of the light beams and a second one emitted into the other light beam. In the unsaturated case discussed here the absolute laser intensities enter as proportionality factors that are equal for all components so that they do not have an effect on the relative line strengths.

4.2 Two-photon matrix element

Following the treatment of two-photon absorption in [64] the two-photon Λ transition amplitude A_Λ can be derived in second-order perturbation theory for stimulated two-photon Λ processes between initial state $|i\rangle$ and final state $|f\rangle$. When keeping only resonant terms one obtains:

$$A_\Lambda \propto \sum_s \frac{\langle f|\,\boldsymbol{d}\times\boldsymbol{E}_2^*\,|s\rangle\,\langle s|\,\boldsymbol{d}\times\boldsymbol{E}_1\,|i\rangle}{\omega_1-\omega_{si}+\mathrm{i}\gamma_s/2}\,. \tag{28}$$

Here $\boldsymbol{d} = -e\boldsymbol{r}$ is the electric dipole operator, $\boldsymbol{r}$ the position vector of the valence electron, $|s\rangle$ are all possible intermediate excited states, ω_1 is the frequency of the light field $\boldsymbol{E}_1$, ω_{si} the frequency difference between states $|s\rangle$ and $|i\rangle$, and γ_s the decay rate of state $|s\rangle$. In the case of the cesium D_2 line discussed here, $|i\rangle = |\,^6S_{1/2},\ F=3,\ m_3\rangle$, $|f\rangle = |\,^6S_{1/2},\ F=4,\ m_4\rangle$, and $|s\rangle = |\,^6P_{3/2},\ F_s,\ m_s\rangle$. The detailed derivation is presented in [65].

With both the dipole operator and the electric light fields,

$$\boldsymbol{E}_1 = E_{10}(a_1\hat{e}_1 + a_0\hat{e}_0 + a_{-1}\hat{e}_{-1})\,, \tag{29}$$

$$\boldsymbol{E}_2^* = E_{20}(b_1\hat{e}_1 + b_0\hat{e}_0 + b_{-1}\hat{e}_{-1})\,, \tag{30}$$

expanded in terms of the standard spherical tensor basis $\{\hat{e}_p\}$ the dipole energy takes the form

$$\boldsymbol{d}\times\boldsymbol{E}_1 = -eE_{10}\sum_{p=-1}^{1}(-1)^p a_{-p} r_p \tag{31}$$

and (28) can be written as:

$$A_\Lambda \propto \sum_s \sum_{p,q}(-1)^{p+q} a_{-p} b_{-q}\frac{\langle f|\,r_q\,|s\rangle\,\langle s|\,r_p\,|i\rangle}{N(\psi, s)} \tag{32}$$

$$\propto \sum_{K=0}^{2}\sum_{Q=-K}^{K}(-1)^Q a^{(K)}_{-Q}\,\langle f|\,R^{(K)}_{\mathrm{Q}}\,|i\rangle\,, \tag{33}$$

where

$$a^{(K)}_{\mathrm{Q}} = \sum_{p,q}\langle 1\ p\ 1\ q|K\ Q\rangle a_p b_q\,, \tag{34}$$

$$R^{(K)}_{\mathrm{Q}} = \sum_s\sum_{p,q}\langle 1\ p\ 1\ q|K\ Q\rangle\, r_p\,|s\rangle\,\langle s|\,r_q\,/N(\psi, F_s)\,, \tag{35}$$

and $N(\psi, F_s) = \omega_1 - \omega_{si} + \mathrm{i}\gamma_s/2$. Here $a^{(K)}_{\mathrm{Q}}$ depends only on the laser polarizations and $R^{(K)}_{\mathrm{Q}}$ contains only atomic quantities. Application of the Wigner–Eckart theorem to $\langle f|\,R^{(K)}_{\mathrm{Q}}\,|i\rangle$ allows us to split off the Q dependence:

$$A_\Lambda \propto \sum_{K,Q}(-1)^{F_f - m_f + Q} a^{(K)}_{-Q}\begin{pmatrix} F_f & K & F_i \\ -m_f & Q & m_i\end{pmatrix}\mathcal{M}^{(K)}\,, \tag{36}$$

where

$$\mathcal{M}^{(K)} = (-1)^{F_i - F_f + K}\sqrt{2K+1}\sum_{\psi, F_s}(-1)^{2F_s}/N(\psi, F_s)$$

$$\times\begin{Bmatrix} F_f & K & F_i \\ 1 & F_s & 1\end{Bmatrix}\langle F_f||r||F_s\rangle\langle F_s||r||F_i\rangle \tag{37}$$

is the multipole amplitude of the coupling with multipolarities $K = 0, 1, 2$ corresponding to scalar, vector, and quadrupole couplings. For coherent population trapping resonances in alkali atom ground states, where $F_f \neq F_i$, the $3j$ symbol in (36) vanishes for $K = 0$: scalar coupling is not possible. From (36) one also sees immediately that for each pair of initial and final states the sum (33) reduces to the two terms with $Q = m_f - m_i$:

$$A_\Lambda \propto a^{(1)}_{-Q} \langle f| R^{(1)}_{\mathrm{Q}} |i\rangle + a^{(2)}_{-Q} \langle f| R^{(2)}_{\mathrm{Q}} |i\rangle \,. \tag{38}$$

For the case of two-photon absorption a similar separation into a sum of tensor products was discussed by Cagnac et al. [66] for the case $\omega_1 = \omega_2$ and by Herrmann et al. [67] for $\omega_1 \neq \omega_2$. The polarization-dependent part was also derived by Bonin and McIlrath [68] in order to study selection rules for two-photon absorption. Yuratich and Hanna [69] found a general expression for multiphoton processes of arbitrary order, based on symmetry arguments, and discussed Raman transitions as a special case.

The beauty of the tensor model lies in the fact that it easily allows us to directly trace the influence of various parameters. Apart from the separation of laser polarizations $a^{(K)}_{\mathrm{Q}}$ from atomic quantities $R^{(K)}_{\mathrm{Q}}$ and $\mathcal{M}^{(K)}$ there are two more aspects.

Geometry. Geometric aspects, i.e., z components breaking spherical symmetry, only enter via $(-1)^Q a^{(K)}_{\mathrm{Q}}$ and the $3j$ symbol. Hence any change in geometry can be accounted for by a rotation of the polarization tensor whereas all the remaining formula remains the same. This applies not only to polarizations but also to changes of the magnetic field direction. If an external magnetic field is not along the laser propagation direction $\hat{e}_z$, all one has to do is to transform the input polarizations into a coordinate system with $\hat{e}_{z'}$ along $\boldsymbol{B}$ (as the quantization axis is chosen along $\boldsymbol{B}$). By definition, for spherical tensors this is done using the rotation matrices $D^{(K)}_{Q\,Q'}$:

$$\tilde{a}^{(K)}_{Q'} = \sum_{\mathrm{Q}} a^{(K)}_{\mathrm{Q}}\, D^{(K)}_{Q\,Q'} \,. \tag{39}$$

Excited states. The properties of the excited states (F_s, γ_s, hyperfine splitting) enter into $\mathcal{M}^{(K)}$ only and it becomes straightforward to account for the influence of a buffer gas. $\mathcal{M}^{(K)}$ can be written as the product of a term $\mathcal{V}(K, F_s)$ depending on the total angular momentum quantum number F_s of the excited state and a term $\mathcal{U}(K)$ containing the F_s-independent terms:

$$\mathcal{M}^{(K)} = \mathcal{U}(K) \sum_{\psi, F_s} \mathcal{V}(K, F_s) \,, \tag{40}$$

$$\begin{aligned}\mathcal{U}(K) = {} & (-1)^{I+L_f+S_f+J_s+L_s+S_s} (2J_s+1)\sqrt{(2K+1)} \\ & \times \sqrt{(2F_f+1)(2F_i+1)(2J_f+1)(2J_i+1)} \\ & \times \begin{Bmatrix} L_f & J_f & S_f \\ J_s & L_s & 1 \end{Bmatrix} \begin{Bmatrix} L_s & J_s & S_s \\ J_i & L_i & 1 \end{Bmatrix} \\ & \times \langle L_f||r||L_s\rangle\langle L_s||r||L_i\rangle \,, \end{aligned} \tag{41}$$

$$\begin{aligned}\mathcal{V}(K, F_s) = {} & (-1)^{F_i+F_s+F_f+I+J_i+J_s+J_f+K} \\ & \times \begin{Bmatrix} F_f & F_s & 1 \\ 1 & K & F_i \end{Bmatrix} \begin{Bmatrix} I & F_s & J_s \\ 1 & J_f & F_f \end{Bmatrix} \\ & \times \begin{Bmatrix} F_i & F_s & 1 \\ J_s & J_i & I \end{Bmatrix} \frac{1}{N(\psi, F_s)} \end{aligned} \tag{42}$$

$$= \mathcal{W}(K, F_s)\,/N(\psi, F_s) \,. \tag{43}$$

In a vapor cell at room temperature the Doppler width of the cesium D_2 line is 370 MHz which is comparable to the hyperfine splittings in the $^6P_{3/2}$ state (Fig. 5). If the laser frequencies are tuned into the hyperfine manifold of the $^6P_{3/2}$ state two different velocity classes are resonant with the transition $|i\rangle \to |s\rangle$ for $F_s = 3$ and for $F_s = 4$. These classes with a width corresponding to the homogeneous width γ_s give the dominant contribution of level F_s to the dark resonance line strength. In an unbuffered cesium vapor the states $|s\rangle$ have a frequency difference much larger than γ_s, so that for each individual atom only one F_s level will effectively enter into S_{rel} because for the other level the optical detuning is too large. In a buffer gas, however, γ_s is strongly collisionally broadened, and for each atom both F_s levels must be included. Therefore, apart from using the appropriate value of γ_s, the model accounts for the buffer gas by performing the summation over all possible excited states for transition *rates* (no buffer gas):

$$\begin{aligned} S^{\text{no buffer gas}}_{\mathrm{rel}} \propto \sum_{F_s} \Bigg| \sum_{K,Q} (-1)^Q a^{(K)}_{-Q} \begin{pmatrix} F_f & K & F_i \\ -m_f & Q & m_i \end{pmatrix} \\ \times\, \mathcal{U}(K)\mathcal{V}(K, F_s) \Bigg|^2 , \end{aligned} \tag{44}$$

or transition *amplitudes* (with sufficiently high buffer gas pressure):

$$\begin{aligned} S^{\text{buffer gas}}_{\mathrm{rel}} \propto \Bigg| \sum_{F_s} \sum_{K,Q} (-1)^Q a^{(K)}_{-Q} \begin{pmatrix} F_f & K & F_i \\ -m_f & Q & m_i \end{pmatrix} \\ \times\, \mathcal{U}(K)\mathcal{V}(K, F_s) \Bigg|^2 . \end{aligned} \tag{45}$$

When the summation is over amplitudes (45), interference effects can play an important role. In fact, the model shows that at sufficiently high buffer gas pressure, i.e., large γ_s, the $K = 2$ contributions cancel: in a buffer gas no quadrupole coupling is possible. This can be seen the following way: With $\delta_i = \omega_1 - \omega_{si}(F_s = F_i)$ and $\delta_f = \omega_1 - \omega_{si}(F_s = F_f)$ the summation over the two possible values of F_s can be written as

$$\begin{aligned} \sum_{F_s} \mathcal{V}(K, F_s) = {} & \mathcal{W}(K, F_i) \frac{\delta_i - \mathrm{i}\gamma_s/2}{\delta_i^2 + \gamma_s^2/4} \\ & + \mathcal{W}(K, F_f) \frac{\delta_f - \mathrm{i}\gamma_s/2}{\delta_f^2 + \gamma_s^2/4} \,. \end{aligned} \tag{46}$$

For large γ_s the terms δ_i^2 and δ_f^2 in the denominators quickly become negligible:

$$\sum_{F_s} \mathcal{V}(K, F_s) = \frac{4}{\gamma_s^2}\big[\delta_i \mathcal{W}(K, F_i) + \delta_f \mathcal{W}(K, F_f)\big] - \mathrm{i}\frac{2}{\gamma_s}\big[\mathcal{W}(K, F_i) + \mathcal{W}(K, F_f)\big]. \quad (47)$$

After some angular momentum algebra one finds that the imaginary part vanishes for $K = 2$ (for details see [65]) so that the transition amplitude scales like γ_s^{-2} and the line strength like γ_s^{-4}. In contrast, for $K = 1$ the imaginary part does not vanish but in general dominates because of its γ_s^{-1} dependence for the amplitude and γ_s^{-2} for the rate. Therefore the $K = 2$ contribution to the transition amplitude decreases with increasing γ_s and becomes negligible, for example, above a few kPa of neon in cesium vapor. A similar argument was given by Happer and Mathur [70] for the case of one-photon optical pumping of atoms with a hyperfine splitting smaller than the Doppler broadening.

4.3 Experimental test of the multilevel model

4.3.1 Line strengths in a magnetic field. The dependence of the relative line strengths on magnetic field direction is illustrated in Fig. 12 with a series of spectra recorded with identical circular laser polarizations in a cell with 8.7 kPa of neon as buffer gas. At such a high pressure only the $K = 1$ component effectively contributes to the coupling. When β is increased the seven even-numbered resonances seen at low β gradually vanish while the eight odd-numbered resonances continually grow until, for β approaching 90°, they alone make up the spectrum.

For a quantitative comparison with the theoretical model the total strength of each component was determined by performing a "running sum" on the raw spectra in Fig. 12, i.e., for each frequency the intensities of all data points to the left of it are summed. The result is a series of lines with absorptive shapes whose areas can be determined by integration. This area is taken as a measure of the relative line strengths.

The spectra in Fig. 12 can be used to check two different predictions of the model: the angular dependence of the fraction of overall line strength contained in the even or odd peaks and the relative strength of different peaks for a fixed β.

Total line strengths. In this experiment both light beams are σ^+ polarized with respect to a magnetic field along their propagation direction $\hat{e}_z$ ($\beta = 0$). After a rotation by β around the y axis the polarization tensor components are

$$\begin{aligned}
&\tilde{a}_2^{(2)} = -\tfrac{1}{4}\sin^2\beta\,, \\
&\tilde{a}_1^{(2)} = -\tfrac{1}{4}\sin 2\beta\,, && \tilde{a}_1^{(1)} = -\tfrac{1}{2}\sin\beta\,, \\
&\tilde{a}_0^{(2)} = \tfrac{1}{\sqrt{6}}(\tfrac{3}{2}\sin^2\beta - 1)\,, && \tilde{a}_0^{(1)} = -\tfrac{1}{\sqrt{2}}\cos\beta\,, \\
&\tilde{a}_{-1}^{(2)} = \tfrac{1}{4}\sin 2\beta\,, && \tilde{a}_{-1}^{(1)} = \tfrac{1}{2}\sin\beta\,, \\
&\tilde{a}_{-2}^{(2)} = -\tfrac{1}{4}\sin^2\beta\,.
\end{aligned} \quad (48)$$

For $\beta = 0°$ only the $Q = 0$ components do not vanish so that only even-numbered peaks are allowed; this is the situation depicted in Fig. 11a. For $\beta = 90°$ all 15 possible components are present in a cell without buffer gas while in a buffered cell like here, where $K = 2$ does not occur, only odd-numbered peaks ($|Q| = 1$) remain.

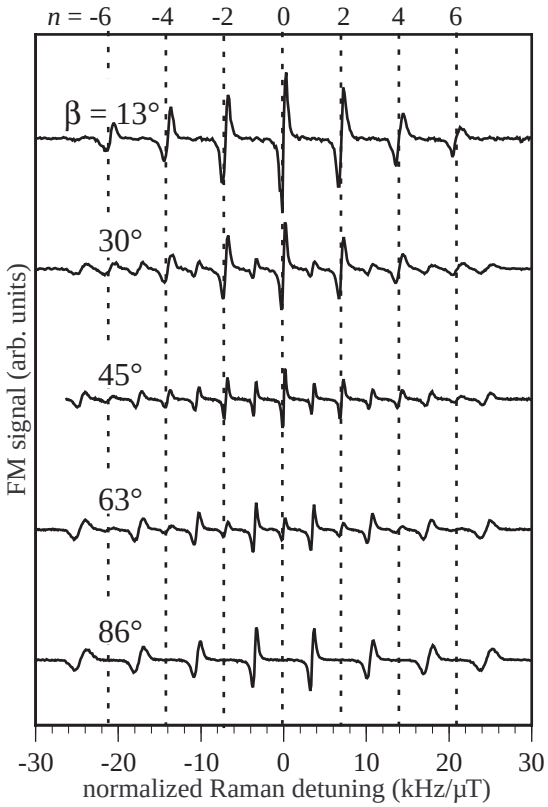

Fig. 12. Dark resonance spectra for $\sigma^+\sigma^+$ excitation and different angles β between laser beam and external magnetic field ($B \approx 10\,\mu$T, 8.7 kPa Ne buffer gas). The *dispersive line* shapes are due to the lock-in detection

The transition rates vary with the square of the probability amplitudes so that here one obtains in the limit of high buffer gas pressure:

$$S_{\mathrm{rel}}^{\text{buffer gas}} \propto \cos^2\beta \quad \text{for } Q = 0\,, \quad (49)$$

$$S_{\mathrm{rel}}^{\text{buffer gas}} \propto \sin^2\beta \quad \text{for } Q = \pm 1\,. \quad (50)$$

The strengths of the even-numbered resonances are therefore expected to decrease as $\cos^2\beta$ while those of odd-numbered resonances should increase as $\sin^2\beta$.

For each of eight spectra for different β, five of which are shown in Fig. 12, the sum S_{even} of the strengths S_{2j} of the seven even-numbered resonances and the sum S_{odd} of the eight odd-numbered resonances S_{2j+1} were normalized to the total strength $S = S_{\mathrm{even}} + S_{\mathrm{odd}}$ (squares and circles in Fig. 13). The solid line represents the pure $\cos^2\beta$ and $\sin^2\beta$ dependencies anticipated from (49) and (50). While there is qualitative agreement there are small systematic differences: the squares are mostly too low and therefore the circles too high. Such a systematic deviation could be due to a spurious magnetic field component in the y direction.

Relative line strengths. At a buffer gas pressure of 8.7 kPa the resonance denominators $N(\psi, F_s)$ are mainly determined by the collisionally increased γ_s, as discussed above. It is therefore possible to simplify the calculations by treating $N(\psi, F_s)$

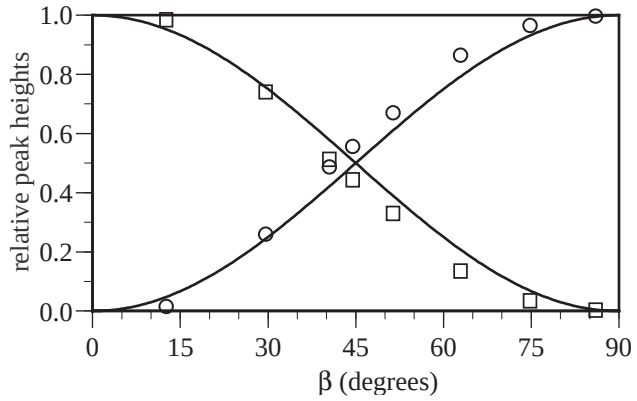

Fig. 13. Measured resonance strengths for the 7 "longitudinal" peaks (*squares*) and the 8 "transverse" peaks (*circles*), cf. Fig. 12, normalized to the total strength of all resonances. The *solid lines* correspond to $\cos^2\beta$ and $\sin^2\beta$

as a constant and by omitting it from (37) for a calculation of relative line strengths (for mathematical details see [65]). The results for circular light polarizations are shown in Fig. 14 as dots connected by solid lines (to guide the eye). For completeness the slightly better results of the full calculation using (37) including the resonance denominators $N(\psi, F_s)$ with $\gamma_s = 2\pi \times 300\,\mathrm{MHz}$ are shown as dashed lines. The value of γ_s was estimated from a fit of Voigt profiles to the Doppler-broadened absorption profile of the buffered vapor cell. The experimental and theoretical spectra have each been normalized to a total line strength of unity. The good agreement justifies the omission in the theoretical model of interaction effects between different Λ systems with shared lower levels.

For $\beta = 86°$ the outermost lines are the strongest components (columns in Fig. 14) although in Fig. 12 they have the smallest height. This purely visual effect is due to field inhomogeneities which broaden the lines at the expense of their heights while leaving the peak areas constant.

4.3.2 Change of multipolarity. The circular polarization used to record the spectra shown in the previous figures is produced with a quarter-wave plate whose optic axis is aligned along the *x* axis. The direction of the linear input polarization makes an angle of $\varphi = 45°$ with the *x* axis (Fig. 15a). When φ is reduced from 45° to 0° the polarization gradually changes from circular to linear:

$$\boldsymbol{E}_1 = E_{10}(\cos\varphi \times \hat{e}_x + i\sin\varphi \times \hat{e}_y) \tag{51}$$

$$= E_{10}\big((\cos\varphi - \sin\varphi) \times \hat{e}_x - \sqrt{2}\sin\varphi \times \sigma^+\big) \tag{52}$$

and similarly for $\boldsymbol{E}_2^*$, resulting in the following non-zero $\tilde{a}_Q^{(K)}$:

$$\tilde{a}_2^{(2)} = \frac{1}{2}\cos 2\varphi\,,$$

$$\tilde{a}_0^{(2)} = -\frac{1}{\sqrt{6}}\,, \qquad \tilde{a}_0^{(1)} = \frac{1}{\sqrt{2}}\sin 2\varphi\,,$$

$$\tilde{a}_{-2}^{(2)} = \frac{1}{2}\cos 2\varphi\,. \tag{53}$$

In a buffer gas, where only $K = 1$ contributes, the line strength should thus depend on φ like $\sin^2 2\varphi$. This was checked experimentally in three cesium cells with different

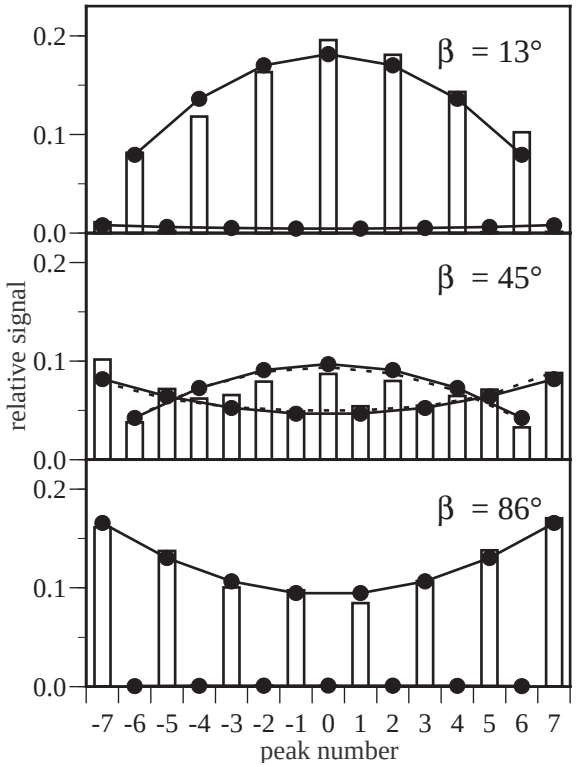

Fig. 14. Comparison of measured (*columns*) and calculated (*dots*) resonance strengths for selected spectra of Fig. 12. The *dashed lines* for $\beta = 45°$ correspond to a complete calculation using (36) with $\gamma_s = 2\pi \times 300\,\mathrm{MHz}$ while for the *dots* (connected by *solid lines*) the limit of high buffer gas pressure was used

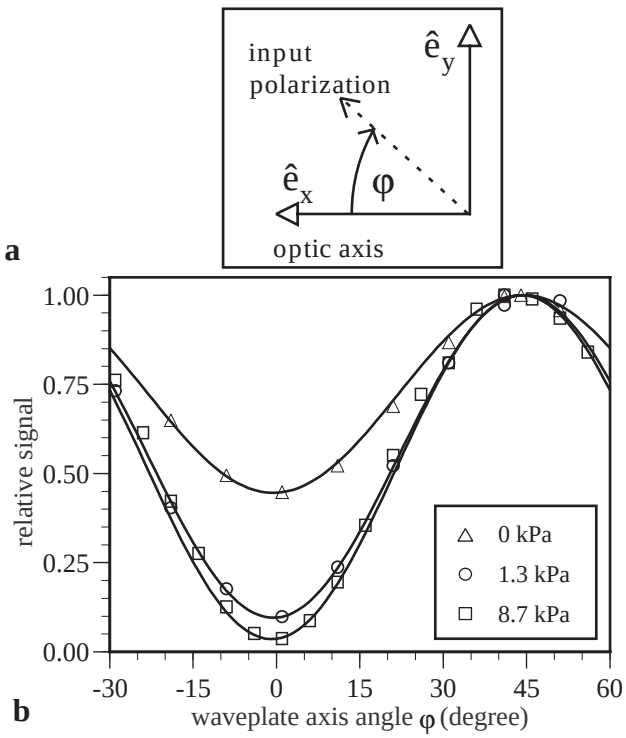

Fig. 15. Dependence of resonance strength on laser polarization in zero magnetic field for different neon pressures. $\varphi = 45°$: circular, $\varphi = 0°$: linear polarization. The *solid line* is a numerical fit with a $\sin^2 2\varphi$ dependence on top of a constant offset

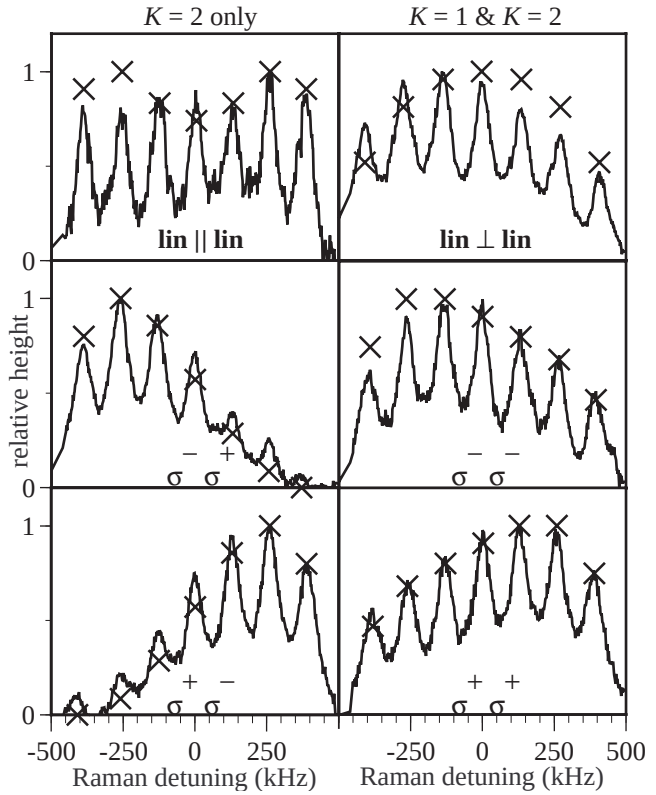

Fig. 16. Polarization dependence of line strengths in a cesium cell without buffer gas (*crosses*: calculated values). The highest peak in each spectrum was normalized to unity (experimental data taken from [44])

Ne pressure at zero magnetic field. In Fig. 15b the normalized total line strength of the dark resonance is plotted as a function of polarization angle φ. The solid lines are numerical fits of an $A + (1 - A)\sin^2 2\varphi$ dependence.

From the fit one obtains $A = (0.45,\ 0.095,\ 0.036)$ for pressures $(0,\ 1.3,\ 8.7)$ kPa, respectively. This confirms the gradual change in multipolarity implied by (47) and might be a way to determine γ_s as a function of pressure without actually having to measure lifetimes or detailed line shapes.

4.3.3 Polarization dependence in pure cesium vapor. The spectra for various polarization configurations in a cesium vapor without buffer gas [44] can be reproduced quantitatively (Fig. 16). Small deviations between experiment and theory can be explained by an imperfect "quarter"-wave plate. The polarization configurations for the three spectra on the left of Fig. 16 correspond to pure quadrupole coupling ($K = 2$); in cells with buffer gas no spectra can be seen under these conditions. The three spectra on the right of Fig. 16 have both $K = 1$ and $K = 2$ contributions. This is the reason why the relative line strengths here are different from the spectra for $\sigma^+\sigma^+$ configuration in buffer gas cells (see Figs. 12, 14) where only $K = 1$ contributes.

5 Precision measurements

Since the dark resonance lines obtained with the help of coherently coupled lasers are so narrow (Fig. 9) a very precise determination of their position or of changes in those positions due to external influences is possible. For instance, Zeeman shifts of the dark resonance lines can be detected even for very weak external magnetic fields. In a strong magnetic field, on the other hand, the positions of the Zeeman components of the dark resonance not only reflect the electronic but also the nuclear magnetic moment of the cesium ground states. With proper analysis the ratio g_I/g_J of nuclear to electronic g-factors can be extracted. If, in contrast, the vapor cell is shielded from external influences the position of the undisturbed resonance can serve as a frequency marker, thus forming the basis of a compact atomic clock.

Apart from the attainable precision (i.e., the number of significant digits or the sensitivity, depending on context) the possible accuracy (i.e., the "correctness" of the numerical value) and reproducibility are important. Before particular applications can be discussed in detail one has to study systematic effects that shift the coherent population trapping resonance.

5.1 Basics of precision measurements

Apart from the control of systematic effects the main experimental problem in precision measurements is how to maximize the signal-to-noise (S/N) ratio without sacrificing sensitivity. The experimental applications discussed below all rely on the sensitive detection of resonance line positions. The smallest line shift $\Delta f_{\min}$ that can be detected is given by the smallest detectable signal change $\Delta S_{\min}$ in the presence of noise in relation to the steepness $\mathrm{d}S/\mathrm{d}f$ of the line, i.e., the change in signal for a small shift of the line:

$$\Delta f_{\min} = \frac{\Delta S_{\min}}{\mathrm{d}S/\mathrm{d}f}\,. \tag{54}$$

The signal detection limit is reached at $S/N = 1$ so that $\Delta S_{\min}$ corresponds to the noise level. Obviously it is best to choose the point of steepest slope (maximum $\mathrm{d}S/\mathrm{d}f$) of the line shape as operating point. $\mathrm{d}S/\mathrm{d}f$ itself can be optimized in two ways: by reducing the width of the resonance or by increasing its height.

Not only the narrow linewidths of the coherent population trapping resonance makes it a good candidate for precision measurements but also the fact that the resonance is "dark", i.e., there is no absorption at line center. The ideal precision experiment with a dark resonance would therefore detect the phase shift near the center of the resonance which provides a steep slope (see Fig. 2). This slope can be greatly increased by heating the vapor cell so that the density of interacting particles becomes higher. While near a "bright" resonance the medium would become optically thick so that no more light reaches the detector, it remains transparent near a dark resonance.

In order to maximize the S/N ratio one has to study the characteristics of the noise sources influencing the particular experiment. Since some important noise sources have spectral densities that drop with increasing Fourier frequencies, for example, $1/f$ noise, a modulation technique is usually superior to pure dc detection. Many noise contributions are independent of the signal level; their influence can therefore be suppressed for high enough signal levels where signal-dependent noise processes dominate, the most important of which is detector shot noise.

In the absence of systematic background effects the shot-noise level usually forms the ultimate sensitivity limit for an optical detection scheme. Shot noise is due to the statistical nature of the photodetection process and is usually quantified by the rms fluctuations I_{shot} of the photocurrent I_{photo}, measured in a bandwidth b:

$$I_{\text{shot}} = \sqrt{2eI_{\text{photo}}b}\,. \tag{55}$$

If all other noise sources can be neglected the S/N ratio of an optical detector,

$$S/N = \frac{I_{\text{photo}}}{I_{\text{shot}}} = \sqrt{\frac{I_{\text{photo}}}{2eb}}\,, \tag{56}$$

increases with the square root of I_{photo}. Naively it seems best to use as much optical power as possible before the detector saturates in order to increase the S/N ratio. However, increasing optical power in general leads to saturation broadening of the optical resonance (Fig. 10) so that there is an optimum intensity as a trade-off between S/N ratio and line steepness.

This optimum can be found experimentally for coherent population trapping resonances in buffered and unbuffered cesium cells. The steepness of the line is proportional to $I_{\text{photo, max}}/\text{FWHM}$ so that in the shot-noise limit

$$\Delta f_{\text{min}} \propto \frac{\text{FWHM}}{\sqrt{I_{\text{photo, max}}}}\,. \tag{57}$$

The reciprocal of this quantity is plotted in Fig. 17 [6]. A sensitivity improvement of a factor of 25 can thus be gained in buffered cells as compared to unbuffered ones. For cesium about 2 kPa of neon is the optimum buffer gas pressure (Fig. 18).

Although the group index (i.e., the steepness of the dispersion curve) has not yet been measured directly for buffered cells one can estimate it using the ratio $I_{\text{photo, max}}/\text{FWHM}$. A comparison for the data of Fig. 17 gives an increase of this quantity by a factor of 16 due to the buffer gas. Assuming $n_{\text{g}} = 3400$ for the case without buffer gas [15] one obtains $n_{\text{g}} \approx 55\,000$ which translates into a group velocity roughly equal to the speed of sound in glass.

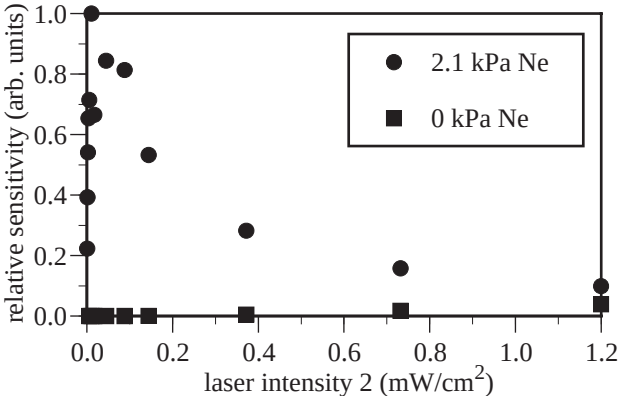

Fig. 17. Sensitivity according to (57) for the detection of small shifts in the dark resonance position as a function of intensity

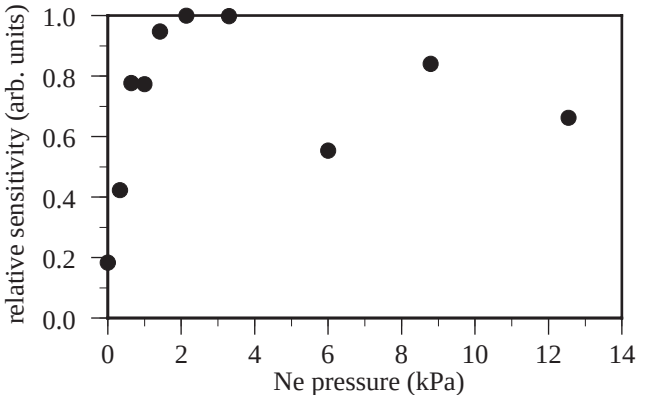

Fig. 18. Buffer gas pressure dependence of the sensitivity for the detection of small shifts in the dark resonance position

5.2 A collection of frequency-shifting effects

In order to simplify the discussion of systematic effects it is convenient to keep an atomic frequency standard as a specific example in mind (Sect. 8). The results can easily be transferred to the other precision measurements discussed in this paper.

The general idea of an atomic frequency standard is to stabilize an oscillator (in the case of coherent population trapping resonances the rf generator that determines the laser difference-frequency) such that the signal from the atomic resonance line remains constant. In the simplest case this could be a point at half the height of the transmission peak (dashed line in Fig. 19). Two types of frequency-shifting effects can be distinguished.

In the first type a shift of the center of the resonance line leads to a corresponding shift of the lock point (Fig. 19a). The second type of shift is less obvious. When the resonance line is broadened without a change in total strength the concomitant change in line shape can lead to a shift of the lock point. In Fig. 19b this is illustrated for a Lorentzian line shape

$$\mathcal{L}(\delta) = \frac{1}{\pi}\frac{\Gamma}{\delta^2 + \Gamma^2} \tag{58}$$

with a half width Γ at half maximum, a total peak area of unity, detuning δ, and $\mathcal{L}(\Gamma) = 1/2\pi\Gamma$. If for some reason the width Γ changes, the point with height $1/2\pi\Gamma$, i.e., the locking point, moves.

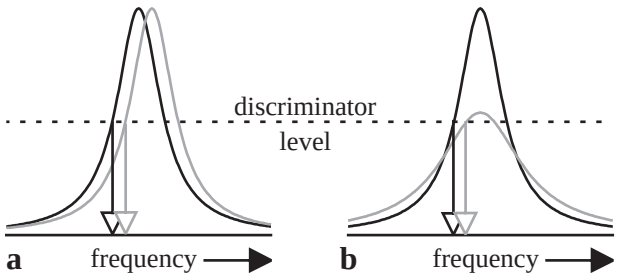

Fig. 19a,b. Two types of effects can shift the frequency of an oscillator locked to a constant signal level (*dashed line*) at the side of an atomic resonance line. **a** Shift of the line center. **b** Change of linewidth at constant peak area

The broadening mechanisms can be classified according to whether they leave the total line strength constant (like magnetic field inhomogeneities) or not (like power broadening). Both types can be modeled by the modified line shape

$$\tilde{\mathcal{L}}(\delta) = \frac{1}{\pi}\frac{\Gamma u^{\eta}}{\delta^2 + \Gamma^2 u^2}\,, \tag{59}$$

where u is a dimensionless linewidth broadening factor and $\eta = 0$ for power broadening and $\eta = 1$ for line strength-preserving broadening. The new position of the point at height $1/2\pi\Gamma$ is $\delta' = \Gamma\sqrt{2u^{\eta} - u^2}$, corresponding to a relative shift of $1 - \delta'/\Gamma = 1 - \sqrt{2u^{\eta} - u^2}$ (Fig. 20). Since the power broadening of the dark resonance line is proportional to intensity (Fig. 10) the broadening factor can be written as $u = 1 + bI/\Gamma$. For a cell with the optimum neon pressure of 2 kPa (Fig. 18) the width increases at a rate $b = 4.1\,\mathrm{kHz/(mW/cm^2)}$. A Taylor expansion around the optimum intensity $I_{\mathrm{opt}} = 0.01\,\mathrm{mW/cm^2}$ (Fig. 17) allows us to estimate a shift rate of $34\,\mathrm{Hz/(mW/cm^2)}$, corresponding to 3.4 mHz shift for a 1% fluctuation in laser intensity which might require an active intensity stabilization of the laser source for some applications.

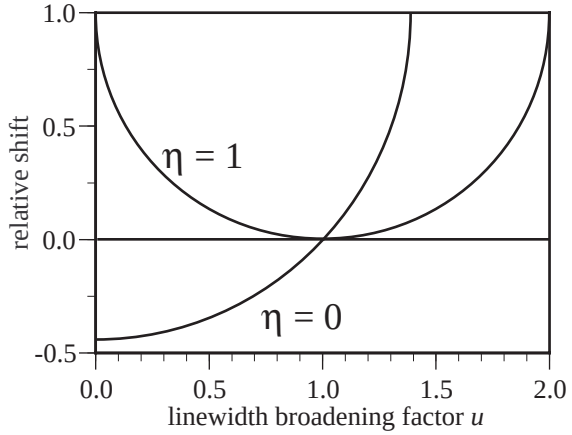

Fig. 20. Shift of the lock point versus broadening factor u for a Lorentzian line shape, normalized to the unbroadened linewidth

5.2.1 Buffer gas pressure. With the help of an inert buffer gas such as neon the effective interaction time between cesium atoms and light can be increased greatly, leading to very narrow resonance lines (Figs. 8 and 9). Whereas collisions with neon atoms have only a very small probability of destroying the ground state coherence they nevertheless influence it. In a simplified picture two regimes have to be distinguished while a cesium and a neon atom are approaching each other during a collision. At large interatomic separations the van der Waals interaction tends to pull the cesium valence electron away from the core while at small separations it is pushed closer. Since neon is only weakly polarizable the van der Waals interaction is small and the net effect of the collision is an increase of the hyperfine interaction, i.e., a blueshift of the coherent population trapping resonance (Fig. 21).

The shift increases at a rate of $(4.80 \pm 0.10)\,\mathrm{Hz/Pa}$ [6]. This is in agreement with a value of $(4.52 \pm 0.2)\,\mathrm{Hz/Pa}$ determined by Beverini et al. [71] for the rf transition between the two lower states. Changes in buffer gas pressure can therefore cause comparatively large systematic shifts. For instance, using the equation of state for an ideal gas a temperature rise of 1 K for a sealed-off cell with 2 kPa neon increases the resonance frequency by 32 Hz.

The influence of buffer gas pressure variations can largely be compensated when a mixture of different gases is used. For heavier and easier polarizable noble gases such as Ar or Kr the pressure shift rate is negative due to the dominance of the van der Waals interaction during the collision [50]. A mixture of 38% neon and 62% argon should therefore lead to a cancellation of the buffer gas shift while the line should broaden by a factor of 2 to 8 (depending on which of the published relaxation cross sections of the rf transition is correct). The broadening leads only to a slight decrease in sensitivity because the estimate for Fig. 17 shows that the best sensitivity for a neon-buffered cell is reached at a laser intensity where the line is already slightly power-broadened.

Another interesting phenomenon is a change in the g_J-factor of the electron due to the net effect of the buffer gas collisions. This could affect the line positions in a magnetic field. Herman [72] has calculated a change of

$$\frac{\Delta g_J}{g_J} = -\sqrt{\frac{4}{3\pi}}\, N_{\mathrm{buff}}\sigma_{\mathrm{kin}}\sqrt{\sigma_{\mathrm{dis}}}\,, \tag{60}$$

where N_{buff} is the number density of buffer gas atoms, σ_{kin} the kinetic cross section, and σ_{dis} the electron randomization cross section due to the interaction between electron spin and the relative angular momentum of the collision partners. There has been unpublished work at the former National Bureau of Standards in Boulder [73] where a relative change $(\mathrm{d}g_J/\mathrm{d}p)/g_J = -(3.95 \pm 0.11) \times 10^{-13}\,/\mathrm{Pa}$ for rubidium in helium was found after a correction for the diamagnetism of helium, in accordance with Herman's theory. Kristensen et al. [74] find changes in the Faraday effect at high buffer gas pressure which could also be accompanied by changes in g_J. Assuming that the same pressure dependence as for rubidium in helium also holds for cesium in neon, the effect of a change in g_J with pressure would only give a negligible contribution of about $10^{-8}\,\mathrm{Hz/(\mu T\,Pa)}$ in small fields for the outermost ($n = \pm 7$) components of the dark resonance. The 0-0 component will be affected even less.

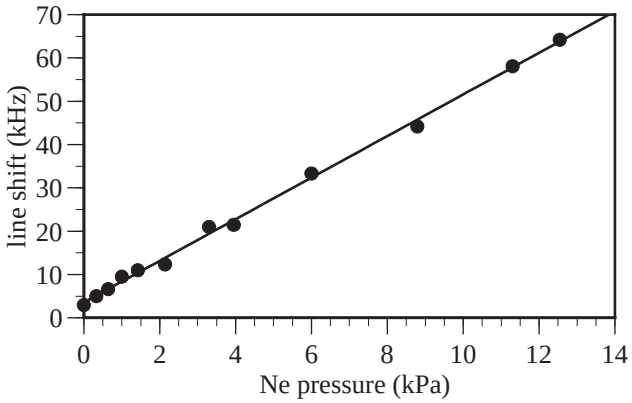

Fig. 21. Shift of dark resonance position versus neon pressure

5.2.2 Light shift. The presence of a resonant light field not only induces transitions between two atomic states but also shifts the relative position of the two energy states through the dynamic (ac) Stark effect. This light shift is proportional to the light intensity and to the strength of the transition. Because on resonance the dark state $|-\rangle$ according to (13) does not couple to the light fields its position is independent of light intensity. However, it is well known that the minimum absorption occurs for a small Raman detuning δ_R away from the position of the dark state [12], and the position of this minimum depends on light intensity. For precision measurements this shift is a very important aspect to understand and control.

In the experiment the light shift was measured with the usual setup for a cell containing no buffer gas (Fig. 6). With both lasers circularly polarized the one-photon detuning $\delta_L = \omega_2 - \omega_{32}$ was held constant by stabilizing laser frequency ω_2 to the Doppler-broadened absorption profile in an auxiliary cesium vapor cell, at a frequency position near the crossover transition from the $F = 4$ ground state to the excited $F = 3$ and $F = 4$ levels. In order to exclude additional frequency shifts from spurious magnetic fields a longitudinal magnetic flux density of 24 μT was applied. Accordingly, the dark resonance split into seven Zeeman components, of which only the one corresponding to the coupling of $|\,^6S_{1/2},\ F = 3,\ m_F = 0\rangle$ and $|\,^6S_{1/2},\ F = 4,\ m_F = 0\rangle$ was considered because it only shifts to second order in B. The intensity of laser 2 was varied from 0.6 μW/cm^2 to 1.2 mW/cm^2 (about the saturation intensity of the optical one-photon transitions) while the intensity of the other laser was always a factor of 2/3 lower. These intensities correspond to the most interesting range for precision applications because for higher intensities the sensitivity is reduced by power broadening of the resonance [6]. For each intensity a frequency modulation spectrum of the dark line was recorded and subsequently its position was determined from a numerical fit assuming Lorentzian line shapes. Figure 22 shows the experimentally determined dependence on intensity together with a zero-parameter curve resulting from a rather straightforward theoretical model to be described in the following.

The shape of the transmission curve for a low-density vapor is basically given by the imaginary parts $n_1''(\delta_R)$ and $n_2''(\delta_R)$ of the refractive indices at the two optical transitions

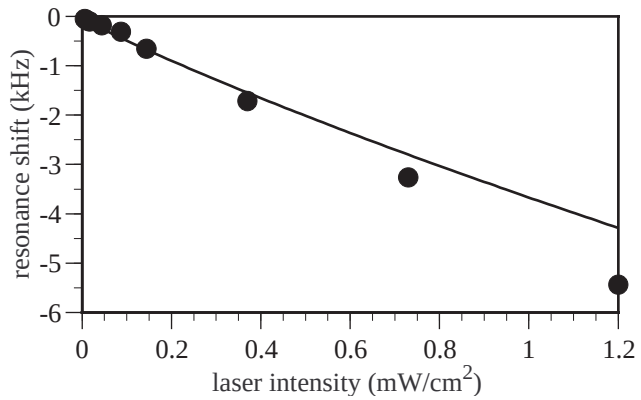

Fig. 22. Comparison of the theoretical dependence (*solid line*) of the dark resonance shift on the laser intensity of the stronger laser with the experimental data points. There is no free parameter in the theoretical model

$|1\rangle$–$|3\rangle$ and $|2\rangle$–$|3\rangle$:

$$I_{\rm tot}(\delta_R) = I_{01}\exp\left(-2kn_1''(\delta_R)l\right) + I_{02}\exp(-2kn_2''(\delta_R)l) \quad (61)$$

$$\approx I_{01} + I_{02} - 2kl\left(I_{01}n_1''(\delta_R) + I_{02}n_2''(\delta_R)\right). \quad (62)$$

Here I denotes intensity, k is the wavevector, and l the length of the optically thin vapor cell. In'' is connected to the excited state population n_3 by

$$I_{01}n_1'' = \hbar c N g_1 Im\left\langle |1\rangle\langle 3|\right\rangle/4 = \hbar c N\gamma_1 n_3(\delta_L, \delta_R)/4\,, \quad (63)$$

$$I_{02}n_2'' = \hbar c N g_2 Im\left\langle |2\rangle\langle 3|\right\rangle/4 = \hbar c N\gamma_2 n_3(\delta_L, \delta_R)/4\,, \quad (64)$$

where N is the vapor density. The center of the dark resonance line can therefore be obtained from the center of $n_3(\delta_L, \delta_R)$:

$$I_{\rm tot}(\delta_R) = I_{01} + I_{02} - kl\hbar c N(\gamma_1 + \gamma_2)n_3(\delta_L, \delta_R)/2\,. \quad (65)$$

$n_3(\delta_L, \delta_R)$ can directly be taken from (14). This formula exhibits asymmetric line shapes (with respect to Raman detuning) for $\delta_L \neq 0$, and the minimum can be shifted from $\delta_R = 0$. We should note here that this shift is not simply given by the difference of the ac Stark shifts of the two optical transitions, as one might intuitively assume. Instead it is essential to include the ground state coherence into the calculation.

We have not been able to find a completely general formula like (14) in an extensive body of literature on three-level systems [12, 75, 76]. However, many approximate solutions were derived [12]. For example, for the case of a weak field on the $|2\rangle$–$|3\rangle$ transition an expression for the susceptibility was given in [5]; starting from there we find the position of the local minimum of their line shape at $\delta_R = \delta_L\Gamma_{21}/\gamma_2$, which is just the limit obtained from our (14) for $g_2^2 \ll g_1^2$.

In a vapor cell the situation is complicated by the distribution $f_D(\delta)$ of atomic velocities v, causing a Doppler shift of the detunings $\delta_L \to \delta_L + \delta$, $\delta = kv$, for the copropagating light fields:

$$n_D''(\delta_L, \delta_R) \propto \int f_D(\delta)n_3(\delta_L + \delta, \delta_R)\,{\rm d}\delta \quad (66)$$

$$= \int f_D(\delta - \delta_L)n_3(\delta, \delta_R)d\delta\,. \quad (67)$$

This tends to wash out the line shape asymmetry found for a stationary atom. A small asymmetry remains because the shape of n_D'' depends on the offset δ_L of n_3 with respect to the center of the Doppler distribution: the curves $n_3(\delta_L)$ effectively sit on a sloping background.

The experimental situation for cesium vapor is further complicated by the hyperfine structure in the cesium $^6P_{3/2}$ state (Fig. 5). While the ground states $|1\rangle$ and $|2\rangle$ of Fig. 1 can be identified with the cesium $|\,^6S_{1/2},\ F = 3, 4\rangle$ states, the two excited states $|\,^6P_{3/2},\ F = 3, 4\rangle$ can both play the role of state $|3\rangle$. This is taken into account by an incoherent sum of two three-level resonance lines:

$$n_{D,\,\rm tot}''(\delta_L, \delta_R) = n_D''(\delta_{L3}, \delta_R) + n_D''(\delta_{L4}, \delta_R)\,, \quad (68)$$

where δ_{L3} and δ_{L4} correspond to the laser detunings δ_L with respect to the upper levels $F = 3$ and $F = 4$ of an atom at

rest. It was shown above that such an incoherent sum adequately describes the situation in a vapor cell without buffer gas. In our case $\delta_{L3} - \delta_{L4} = \omega_{43}$ where ω_{43} is the hyperfine splitting of the upper levels $F = 4$ and $F = 3$. With laser 2 locked to the cross-over resonance we have $\delta_{L3} = 101\,\mathrm{MHz}$. The $^6P_{3/2}$, $F = 2, 5$ levels lead to off-resonant one-photon excitation that produces additional dephasing of the ground state coherence. For the calculation a total dephasing rate of $\Gamma_{21} = 2\pi \times 10\,\mathrm{kHz}$ was used, corresponding to the minimum linewidth expected for transit time broadening at our laser beam diameter.

Special care has to be taken to map the relaxation rates and Rabi frequencies of the theoretical three-level model to the two three-level subsystems of the cesium multilevel system. As a very rough approach the Rabi frequencies g_1 and g_2 were scaled with the strength of the corresponding one-photon transition between the angular momentum eigenstates of the cesium atom:

$$g_1^2 \mapsto g_1^2 (2J_3+1)(2F_1+1)(2F_3+1) \begin{pmatrix} F_3 & 1 & F_1 \\ -1 & 1 & 0 \end{pmatrix}^2 \times \begin{Bmatrix} J_3 & F_3 & 7/2 \\ F_1 & J_1 & 1 \end{Bmatrix}^2 = g_1^2 W_1(F_3)\,, \tag{69}$$

and similarly for g_2. Here J_3 and F_3 are the electronic and the total angular momentum quantum numbers in the excited state, and $W_1(F_3 = 3) = 3/8$, $W_1(F_3 = 4) = 25/168$, $W_2(F_3 = 3) = 1/24$, and $W_2(F_3 = 4) = 7/24$. Furthermore the proper branching ratios for spontaneous transitions from the excited states $F_3 = 3, 4$ to the lower states $F = 3, 4$ were used to scale the total decay rate of $\gamma_1 + \gamma_2 = 2\pi \times 5.3\,\mathrm{MHz}$:

$$\gamma_2/\gamma_1 = 7/5 \qquad \text{for } F_3 = 4\,, \tag{70}$$

$$\gamma_2/\gamma_1 = 1/3 \qquad \text{for } F_3 = 3\,. \tag{71}$$

The result of the numerical Doppler integration of $n''_{D,\mathrm{tot}}(\delta_L, \delta_R)$ (solid line in Fig. 22) shows good agreement with the experimental data even without the use of any free parameters. Given the well-known experimental difficulties when trying to determine an accurate value of intensity it is surprising that there is only such a small discrepancy. For instance, for the calculations the transverse Gaussian intensity profile of the laser beam was approximated by a rectangular distribution of equal area, and an increase of all intensities by only 25% would make the small difference between experiment and calculation disappear. An additional effect is the dependence of the total shift on optical detuning δ_L. In the experiment δ_L was held constant only to within a few megahertz, causing a small uncertainty in the slope of the curve of a few percent.

However, the model described above only applies to the situation without buffer gas. In the presence of a buffer gas the optical transitions suffer from strong collisional broadening which for several tens of mbar can be of the same order of magnitude as the hyperfine splitting in the $P_{3/2}$ excited state. Hence the model will have to be extended to account for the fact that now both laser fields can coherently couple to both the $F = 3$ and $F = 4$ upper levels. Therefore, performing an incoherent sum as in (68) is no longer a valid approximation. Figure 23 shows the experimentally determined shift rate as a function of buffer gas pressure, obtained by fitting

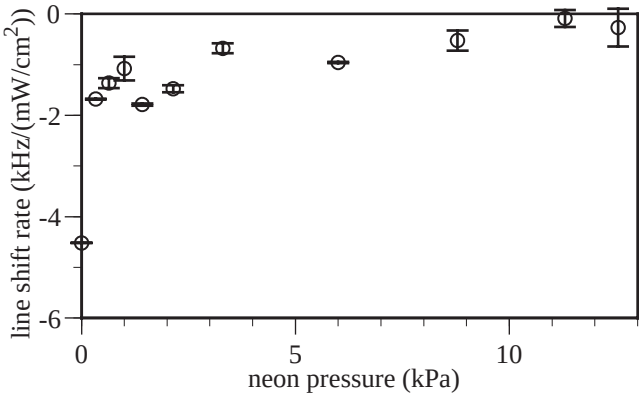

Fig. 23. Slope of the linear approximation for the intensity shift rate of the 0-0 dark resonance component versus neon buffer gas pressure

a straight line to experimental data similar to that in Fig. 22 for each pressure. For instance, at a pressure of about 8 kPa, where the linewidth has its minimum, the light shift rate is reduced already by a factor of 10. So the use of a buffer gas not only reduces the linewidth but also the light shift of the dark resonance.

For precision applications requiring the determination of line positions the intensity-dependent line shifts can be important. For instance, for cesium in neon the optimum sensitivity for Zeeman shifts is reached at an intensity of $0.01\,\mathrm{mW/cm^2}$ and a neon pressure of 2 kPa (Figs. 17, 18). Under these conditions an intensity variation by 1% causes a shift of 0.2 Hz. Depending on the application it might therefore be better to increase the buffer gas pressure in order to reduce the influence of intensity fluctuations.

Not only the laser intensity but also the detuning δ_L of the laser frequency from the optical resonance influences the position of the dark resonance because the relative weights of the contributions of the excited $F = 3$ and $F = 4$ levels change. For instance, using the theoretical model for an unbuffered vapor a reduction of the light shift by more than a factor of 50 is predicted when the lasers are tuned 85 MHz to the blue side of the transitions to the excited $F = 4$ state. Of course, this would be an elegant method to suppress unwanted shifts in precision measurements. Figure 24 shows as an ex-

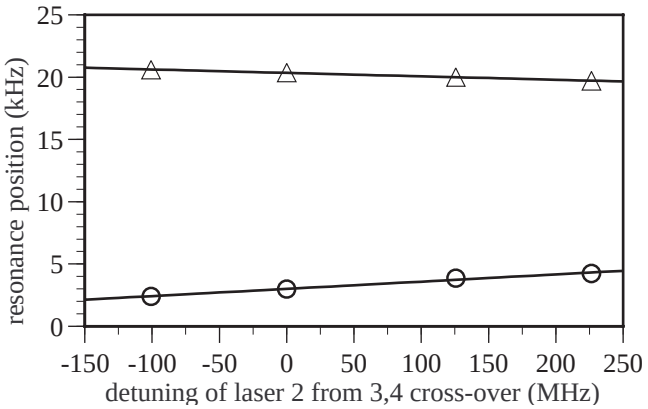

Fig. 24. Position of the dark resonance line center versus detuning of laser 2 from the 3,4 crossover resonance. *Circles*: no buffer gas; *triangles*: 4 kPa neon pressure

ample two measurements without buffer gas and with 4 kPa neon where the position scales with detuning from the (3,4) crossover resonance as 5.8 Hz/MHz and −2.8 Hz/MHz, respectively. Since it is easy to stabilize the laser frequency at the sub-kHz level with respect to a Doppler-free resonance in a saturated absorption spectrum fluctuations of δ_L play a minor role. One could even hope to find a combination of optical detuning and neon pressure where the shift rate vanishes. As discussed before there are, however, other criteria that also influence the optimum choice of buffer gas pressure.

5.2.3 Rotation of the earth. When a spin system is rotated the effect of the rotation is equivalent to an additional magnetic field. So even in a perfectly shielded environment a sensitive magnetometer or a frequency standard will always experience a small magnetic field B_{pseudo} due to the rotation of the earth with angular frequency Ω_{earth}. For a cesium magnetometer locked to resonance number n the total Larmor frequency is given by

$$\omega_{\text{Larmor}} = 2\pi n\xi B + \Omega_{\text{earth}}\,, \tag{72}$$

with $\xi = 3.5\,\text{kHz}/\mu\text{T}$ so that

$$B_{\text{pseudo}} = \Omega_{\text{earth}}/2\pi n\xi = 3.3\,\text{fT}/n \times \cos\phi\,. \tag{73}$$

With the geographical latitude $\phi = 51°$ for Bonn this gives a fictitious field of $B_{\text{pseudo}} = 2.1\,\text{fT/n}$ for the worst possible orientation of the apparatus relative to the rotation axis of the earth, which is negligible except for the most demanding applications.

6 Application 1: magnetometry

There is the common notion that precision and high-sensitivity magnetometry is the exclusive realm of *superconducting quantum interference device* (SQUID) magnetometers. However, similar performance can also be obtained with other types of magnetometers.

A SQUID consists of a superconducting ring with a narrow gap of normal conductivity. The magnetic flux that threads the ring can be measured with very high sensitivity using the Josephson voltages it induces. Even the weak magnetic flux density ($\leq 200\,\text{fT}$) produced by the human brain can be detected with high temporal and moderate spatial resolution [77]. Since a SQUID actually measures magnetic flux the sensitivity to magnetic fields increases with increasing diameter of the flux collection ring while the spatial resolution decreases.

Apart from a more "traditional" way of determining magnetic fields with pick-up coils that can in extreme cases detect flux densities below 1 fT there is the class of optical pumping magnetometers (OPM) that in commercial models routinely reach sensitivities of better than 1 nT in less than a second of integration time. Special adaptations for laboratory applications have been able to detect a 200 fT magnetic flux density produced by spin-polarized nuclei in ^{3}He gas [78]. The current record stands at $1.8\,\text{fT}/\sqrt{\text{Hz}}$ for a potassium magnetometer [79]. Applications range from submarine detection (with undisclosed sensitivities, obviously) to archaeological and geological prospecting and surveying [80]. Although a coherent dark-state magnetometer has a similar principle of operation as an OPM there could be a fundamental difference that should make it two orders of magnitude more sensitive than an OPM. With such a sensitivity it would not only be superior to today's SQUID magnetometers, but it would also have a much better spatial resolution at high sensitivity and would operate at room temperature.

6.1 Measurement principle

In a magnetic field the coherent population trapping resonance is split into several components that are Zeeman shifted at different rates (Fig. 11). This field-dependent shift can be used to determine the strengths of magnetic fields and variations in their strengths with very high sensitivity. For flux densities below 1 T (i.e., when the Zeeman energy is much smaller than the ground state hyperfine splitting) F and m_F are good quantum numbers. For a state $|F = I \pm 1/2, m_F\rangle$ the Breit–Rabi formula gives an energy of

$$E(\pm, m_F) = -\frac{\hbar\Delta_{\text{hfs}}}{16} + m_F\mu_B g_I B \pm \frac{\hbar\Delta_{\text{hfs}}(I+1/2)}{8}\sqrt{1+\frac{4m_F}{2I+1}x+x^2}\,, \tag{74}$$

where $x = 4(g_J - g_I)\mu_B B/\hbar\Delta_{\text{hfs}}(I+1/2)$ and for cesium $I = 7/2$, $\Delta_{\text{hfs}} = 2\pi \times 9.192631770\,\text{GHz}$, $g_J = 2.0025402$ [81], and $g_I = -0.39885395 \times 10^{-3}$ [81], so that $x = 3.0496 \times B/\text{T}$. In the linear Zeeman regime ($x \ll 1$) the dark resonance labeled $n = m_3 + m_4$ shifts with a rate

$$\xi = \frac{\mu_B}{8h}\big(g_J(m_3+m_4) + g_I(7m_4 - 9m_3)\big) \approx 3.51\,\text{kHz}/\mu\text{T} \times (m_3+m_4)\,. \tag{75}$$

For a given linewidth $\Delta\nu$ of the individual components two operating regimes have to be distinguished: strong field ($\Delta\nu \ll \xi B$) and weak field ($\Delta\nu \gg \xi B$).

Strong field. When B is larger than $\Delta\nu/\xi$ the individual components are well separated. Since the line shape does not change with field strength the relative accuracy is independent of B. A fit of the peak positions according to the Breit–Rabi formula (74) gives the value of x, from which B can be calculated. For the spectra in Fig. 25 one obtains $B = (21.2265 \pm 0.0006)\,\mu\text{T}$ and $B = (873.690 \pm 0.028)\,\mu\text{T}$ where the relative uncertainty of about 3×10^{-5} in both cases is that of the numerical fit of the parameter x.

Even with perfect statistics the relative accuracy of this method will be limited to about 2×10^{-6} because the proportionality factor between the fitted parameter x and the calculated B involves the g-factors which are known with a relative uncertainty of 1.3×10^{-6} [81]. However, by setting the laser difference-frequency to the side of one of the resonance lines one could monitor changes of B with a sensitivity of 1 nT or better.

Weak field. When B is smaller than $\Delta\nu/\xi$ the components of the dark resonance overlap, giving rise to a more complicated line shape. The imaginary part n'' of the refractive index $n = n' + \mathrm{i}n''$ of the atomic vapor near the dark resonance can

be modeled as a sum of Lorentzians, weighted with the relative resonance strengths $w_j := S_{\mathrm{rel}}$, as calculated with the help of (36):

$$n''(\omega) = n''_{\mathrm{b}} - n''_0 N \sum_{j=-7}^{7} \frac{w_j (\pi\Delta\nu)^2}{(\delta_{\mathrm{R}} - 2\pi j \xi B)^2 + (\pi\Delta\nu)^2} \,. \tag{76}$$

Here $N = 1/\sum_{j=-7}^{7} w_j$, δ_{R} is the detuning from the dark resonance, n''_{b} is a background absorption index, and n''_0 a measure for the overall strength of the resonance.

During their passage through the medium of length l the input fields $E_{1,2}\exp(\mathrm{i}kl) + \mathrm{c.\,c.}$ acquire an additional exponential factor $\exp(-\delta_{1,2} + \mathrm{i}\Phi_{1,2})$ where $\delta_{1,2} = \omega l n''_{1,2}/c$ and $\Phi_{1,2} = \omega l n'_{1,2}/c$. The transmitted signal detected on a slow photo detector contains only the absorptive part:

$$I = \frac{c\varepsilon_0}{4}\left(E_1^2 \mathrm{e}^{-2\delta_1} + E_2^2 \mathrm{e}^{-2\delta_2}\right) . \tag{77}$$

If we assume for simplicity $E_1 = E_2$ it follows that $\delta_1 = \delta_2$ and

$$I(\delta_{\mathrm{R}}, B) = \alpha \exp\left(\beta \sum_j \frac{w_j (\pi\Delta\nu)^2}{(\delta_{\mathrm{R}} - 2\pi j\xi B)^2 + (\pi\Delta\nu)^2}\right) , \tag{78}$$

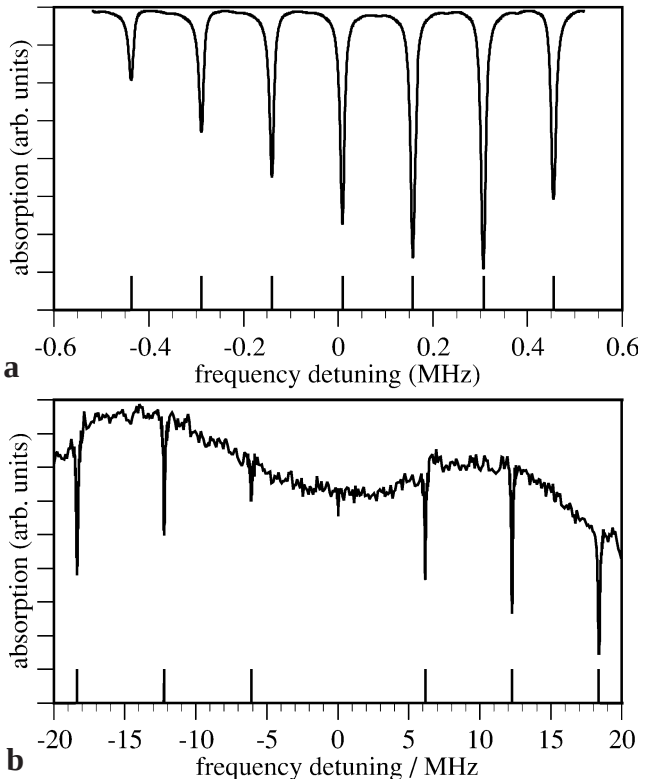

Fig. 25a,b. The magnetic flux density can be determined with better than 3×10^{-5} relative accuracy from a fit of the Breit–Rabi formula to the experimentally determined resonance positions. **a** $B = (21.2265 \pm 0.0006)\,\mu\mathrm{T}$, circular laser polarizations and 8.7 kPa neon buffer gas in a longitudinal field. **b** $B = (873.690 \pm 0.028)\,\mu\mathrm{T}$, parallel linear laser polarizations without buffer gas in a transverse field. The *short vertical lines* indicate the fitted resonance positions

where $\alpha = \dfrac{c\varepsilon_0}{2} E^2 \exp\left(-2\dfrac{\omega}{c} l n''_{\mathrm{b}}\right)$, (79)

$$\beta = 2\frac{\omega}{c} l N n''_0 \,. \tag{80}$$

In first experiments small ac fields were detected using a lock-in amplifier that picks out the Fourier component of the signal oscillating at the amplifier's reference frequency. For a field $B = B_{\mathrm{dc}} + B_{\mathrm{ac}}\cos(\omega_m t)$ a Taylor expansion to first order,

$$I(\delta_{\mathrm{R}}, B) = I(\delta_{\mathrm{R}}, B_{\mathrm{dc}}) + B_{\mathrm{ac}}\cos(\omega_m t)\frac{\mathrm{d}I(\delta_{\mathrm{R}}, B)}{\mathrm{d}B}\Big|_{B_{\mathrm{dc}}} , \tag{81}$$

shows that the lock-in amplifier is mainly sensitive to the first derivative of the line shape (strictly speaking, this is only true if $\omega_m/2\pi$ and ξB_{ac} are much smaller than $\Delta\nu$):

$$S_{\text{lock-in}} = B_{\mathrm{ac}}\frac{\mathrm{d}I}{\mathrm{d}B}\Big|_{B_{\mathrm{dc}}} = 4\pi\xi B_{\mathrm{ac}} I(\delta_{\mathrm{R}}, B)\beta \times \sum_j \frac{j w_j (\delta_{\mathrm{R}} - 2\pi j \xi B_{\mathrm{dc}})}{\left((\delta_{\mathrm{R}} - 2\pi j\xi B_{\mathrm{dc}})^2 + (\pi\Delta\nu)^2\right)^2} \,. \tag{82}$$

Note that $S_{\text{lock-in}} \equiv 0$ for $B_{\mathrm{dc}} = 0$ if the peak height distribution is symmetric ($w_j = w_{-j}$) like, for instance, in a buffer gas for σ^+-polarized lasers. $S_{\text{lock-in}}$ can also be written in terms of absorptive and dispersive Lorentzians:

$$S_{\text{lock-in}} = -\frac{8\xi B_{\mathrm{ac}} I \frac{\omega}{c} l N}{n'_0 \Delta\nu} \sum_j \frac{j}{w_j} \mathcal{L}_{\mathrm{abs}} \mathcal{L}_{\mathrm{disp}} \,. \tag{83}$$

In a demonstration experiment with σ^+-polarized laser beams small longitudinal magnetic fields were applied to a cesium vapor cell using two wire loops in Helmholtz configuration [7]. Then all w_j with odd j are zero and $w_j = \{0.47, 0.68, 0.88, 0.91, 1, 1, 0.75\}$ for $j = \{-6, -4, \ldots, 6\}$. In order to shield the cell from stray fields it was placed inside a long μ-metal cylinder with an estimated longitudinal shielding factor of 1000 (detailed information about the permeability of the μ-metal shield was not available). The dots in Fig. 26 show the absolute value of $S_{\text{lock-in}}$ for $B_{\mathrm{ac}} = 7.2\,\mathrm{pT}$ while the solid line is a numerical fit to the absolute value of (82). From the fit parameters one obtains $\Delta\nu = 40\,\mathrm{kHz}\times(1\pm0.1)$, $n''_0 = 2\times10^{-5}\times(1\pm0.5)$, and $B_{\mathrm{dc}} = -31.6\,\mathrm{nT}\times(1\pm0.084)$, where $\Delta\nu$ is consistent with the expected power broadening for a laser intensity of about $1\,\mathrm{mW/cm^2}$ (Fig. 10) and n''_0 is plausible when compared to the values published in [15].

Since the signal amplitude detected at the maximum of the line shape was found to be proportional to the amplitude of the modulating field one can estimate the possible sensitivity by extrapolating to a S/N ratio of unity. Near the maximum of the line the S/N ratio is about 15 so that one can expect to be able to detect flux densities $B_{\mathrm{ac}} = 7\,\mathrm{pT}/15 \approx 500\,\mathrm{fT}$ within the averaging time of 0.5 s in this case. It is even possible to measure weak dc fields although for that purpose it is necessary to take a full spectrum and analyze the line shape. In principle, however, one could choose a convenient point along the line shape and attribute any changes in signal to a change of B_{dc}. A rough estimate shows that the sensitivity to small dc fields should be comparable to the ac sensitivity – even though the Zeeman components of the dark resonance are not resolved.

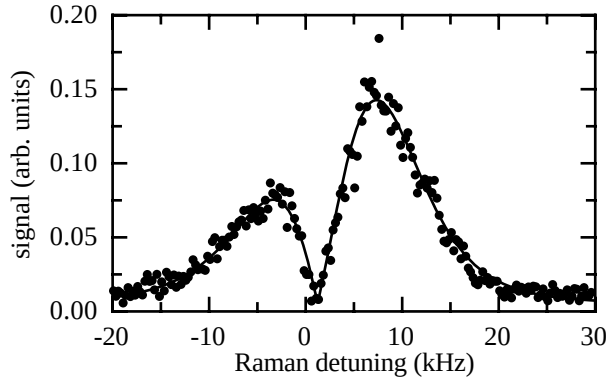

Fig. 26. Line shape for field modulation at 8 kHz with 7 pT amplitude. The *solid line* is a numerical fit using the absolute value of (82)

The detection of the relatively strong dc offset field B_{dc} is an indication that the magnetic shielding is probably also not sufficient for ac fields. It was therefore decided to postpone a more detailed investigation of the dependence of magnetometric sensitivity on modulation frequency and averaging time until a better shielding is available. But even now the result for small ac fields compares favorably with the sensitivity of good OPMs (Fig. 27). The best SQUID systems and OPMs today are, however, still two orders of magnitude more sensitive.

6.2 Advantages of a dark state magnetometer

At first glance, a dark-state magnetometer (DSM) seems very similar to an optical pumping magnetometer (OPM). In an OPM a lamp or a laser optically pumps the atomic population out of state $|2\rangle$ via the excited state $|3\rangle$ into state $|1\rangle$ so that the vapor becomes transparent (see Fig. 1 for notation). Part of the population in $|1\rangle$ can be transferred back into $|2\rangle$ by a magnetic dipole transition induced by an external rf field, leading to a reduced transparency of the vapor. The optimum radio frequency depends on the strength of an external magnetic field via the differential Zeeman shift of $|1\rangle$ and $|2\rangle$. Magnetometers of this type are available commercially. For instance, the Canadian company Scintrex offers a cesium magnetometer operating in a self-oscillating configuration where the transmitted signal of the lamp provides feedback to the rf source [83]. Such a device offers a noise spectral density of $3\,\mathrm{pT}/\sqrt{\mathrm{Hz}}$ for less than $20 000. The best laboratory setup even reaches $1.8\,\mathrm{fT}/\sqrt{\mathrm{Hz}}$ [79].

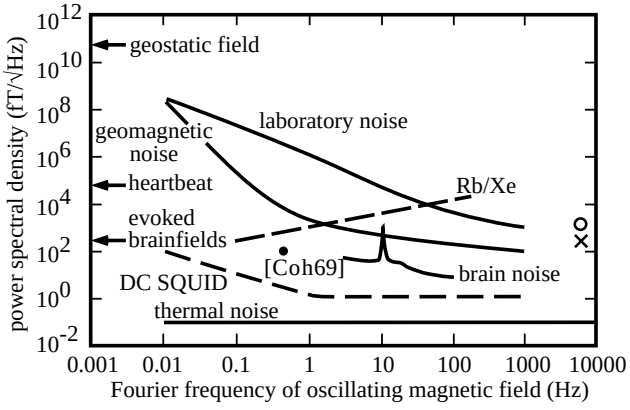

Fig. 27. Typical field strengths of various sources, and typical sensitivities of selected magnetometers. The symbols at 8 kHz Fourier frequency represent the first test experiment (*circle*) and its extrapolation to a S/N ratio of unity (*cross*). "Rb/Xe" stands for a particular type of optical pumping magnetometer [82]

For maximum sensitivity it is useful to increase the lamp or laser intensity in order to reach the shot-noise limit of the detector. However, increasing light intensity also increases the linewidth of the resonance due to saturation. A complete calculation by Scully and Fleischhauer [4, 5] shows that the best sensitivity is reached for a probe Rabi frequency $g_2 \propto \sqrt{\Gamma_{12}\gamma_s}$ where Γ_{12} is the effective dephasing rate between $|1\rangle$ and $|2\rangle$ and γ_s is the decay rate of the optical transition.

The same authors also calculated the sensitivity of a DSM detecting the phase shift near the resonance with a vapor cell in one arm of a Mach–Zehnder interferometer. They found that for large g_1 the probe Rabi frequency can be increased to about $g_2 \propto \sqrt{\gamma_s\gamma_s}$ before power broadening becomes noticeable. Since in the shot-noise limit the sensitivity is inversely proportional to the square root of the power on the detector this means an improvement of a factor $\sqrt{\gamma_s/\Gamma_{12}} > 100$ for buffered vapor cells, pushing the theoretical sensitivity limit below 1 fT in 1 s, i.e., better than today's best SQUID detectors. Future measurements using a sufficiently good magnetic shielding should be able to explore the actual sensitivity limits of a DSM.

Another crucial point for sub-fT sensitivity is the stability of the electronic reference oscillator for the optical phase-locked loop. For a cesium-based setup a relative change of its frequency by 10^{-13} (the stability of the best commercial cesium clocks) is indistinguishable from a change in magnetic field by

$$\Delta B = \frac{\mathrm{d}B}{\mathrm{d}f} \times \Delta f \tag{84}$$

$$= (7 \times 3.5\,\mathrm{kHz}/\mu\mathrm{T})^{-1} \times 10^{-13} \times 9.2\,\mathrm{GHz} = 40\,\mathrm{fT}\,. \tag{85}$$

This effect can be corrected for by a combination of a ^{87}Rb and a cesium magnetometer because the ratio of gyromagnetic factor to hyperfine splitting is different for the two atomic species and therefore allows a discrimination between field changes and oscillator frequency fluctuations.

Possible applications of such an optimized DSM could be the detection of weak biomagnetic fields or experiments searching for parity or time-reversal symmetry-breaking in an atomic system [84].

The recent theoretical result by Grishanin et al. [17] shows another fundamental difference between a magnetometer using Zeeman levels and one using the dark resonance between hyperfine levels. When the three-level system in Fig. 1 is calculated in higher order of the optical interaction so that also four-photon processes are included an additional relaxation mechanism for the (two-photon) coherence between the two lower states appears. The four-photon process can be interpreted as the first higher-order term in a perturbation series for the saturation of the transition and is proportional to the square of the optical intensity. Since it scales

inversely proportional to the square of the frequency separation between $|1\rangle$ and $|2\rangle$ it is negligible for rubidium and cesium hyperfine coherences: at an intensity where the additional relaxation gives a 1 Hz contribution to the linewidth the resonance is already power-broadened to more than 10 kHz by the "usual" first-order term. But for an OPM using a Zeeman transition in the kHz range it can make a large contribution.

7 Application 2: *g*-factor ratio

In the case of a strong magnetic field discussed in Sect. 6 the theoretical maximum for the accuracy of a magnetic flux density determination is given by the uncertainty in the *g*-factors. If these were known perfectly an increase in ultimate accuracy by two orders of magnitude would result, limited by the accuracy of the values of $\hbar$ and μ_B. It is therefore desirable to obtain a better knowledge of the *g*-factors. Since the electronic *g*-factor can also be calculated when the exact wavefunctions are known this would provide a test of wavefunction calculations. Precise knowledge of the wavefunctions, in turn, is important for experiments on the violation of fundamental symmetries in atoms [85–87].

The current knowledge of the *g*-factors in cesium and rubidium stems from a magnetic resonance experiment in the early seventies [81] where accuracies of 1.3×10^{-6} were reached. It turns out that there is an experimental geometry where the ratio g_I/g_J can be determined from the positions of coherent population dark resonances in a strong magnetic field. Although the experiment is currently far from being competitive with the older results it is nevertheless consistent and could offer the same principal advantages as a dark-state magnetometer.

7.1 A proof-of-principle experiment

For equal circular laser polarizations the dark resonance splits into 15 components when a magnetic field is applied at an angle of $\beta = 45°$ with respect to the laser propagation direction (Fig. 28). The even-numbered peaks correspond to couplings with $\Delta m = 0$ and the odd-numbered peaks to $\Delta m = \pm1$. From the Breit–Rabi formula (74) the positions of the dark resonances are given by

$$\Delta f(m_3, m_4) = a(m_4 - m_3) + \frac{\Delta_{\rm hfs}}{4\pi}\left(\sqrt{1+\frac{m_4}{2}x+x^2}+\sqrt{1+\frac{m_3}{2}x+x^2}\right), \tag{86}$$

where $a = g_I\mu_B B/h$. Since the positions of the even-numbered resonances do not depend on a one can numerically fit the peaks with even $n = m_3 + m_4$ to (86) and obtain the optimum value $x_{\rm opt} = (g_J - g_I)\mu_B B/\hbar\Delta_{\rm hfs} = \hbar(g_J/g_I - 1)a_{\rm opt}/\Delta_{\rm hfs}$ and an overall shift $\delta_{\rm buffer}$ due to a buffer gas. $a_{\rm opt}$ follows from a fit of peak positions for odd n with fixed $x_{\rm opt}$ and $\delta_{\rm buffer}$ so that

$$\frac{g_J}{g_I} = 1 + \frac{\Delta_{\rm hfs}}{2\pi}\frac{x_{\rm opt}}{a_{\rm opt}}. \tag{87}$$

From (86) one can see that for $|n| < 7$ each odd-numbered peak actually consists of two components differing only in the nuclear contribution: $|F=3, m_3=(n-1)/2\rangle$ coupled with $|F=4, m_4=(n+1)/2\rangle$, and $|F=3, m_3=(n+1)/2\rangle$ coupled with $|F=4, m_4=(n-1)/2\rangle$. The splitting is $2a$, independent of n, and increases at a rate of $2g_I\mu_B/h = -11.16\,\text{MHz/T}$. The linewidths of about 5 kHz in Fig. 28 are not small enough to resolve the calculated splitting of 120 Hz at $B = 11.1\,\mu$T. Each odd-numbered peak is therefore a superposition of two slightly shifted Lorentzians of different relative heights (Fig. 29). These heights can be calculated using the formalism developed in Sect. 4. At a ratio of splitting to width of 1 : 40 in the present experiment the maximum of the combined unresolved waveform shifts by a negligible amount. For the numerical fit of $a_{\rm opt}$ only the strongest component of each pair was included in the fitting function.

For the spectrum in Fig. 28 one obtains

$$\frac{g_I}{g_J} = -1.87(11)\times10^{-4}, \tag{88}$$

which is consistent with the literature value of $g_I/g_J = -1.9917400(26)\times10^{-4}$ [81] but much less precise.

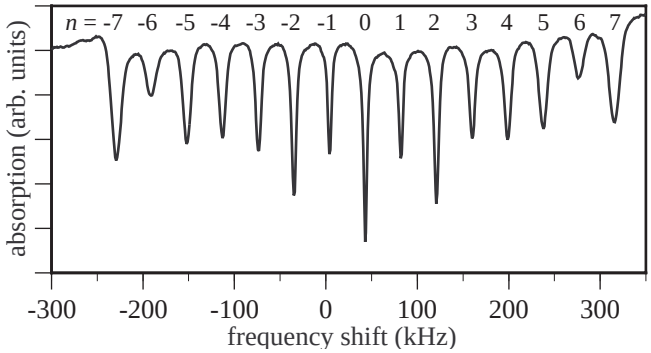

Fig. 28. The 15 dark resonances obtained for oblique magnetic field measured at $B = 11.1\,\mu$T

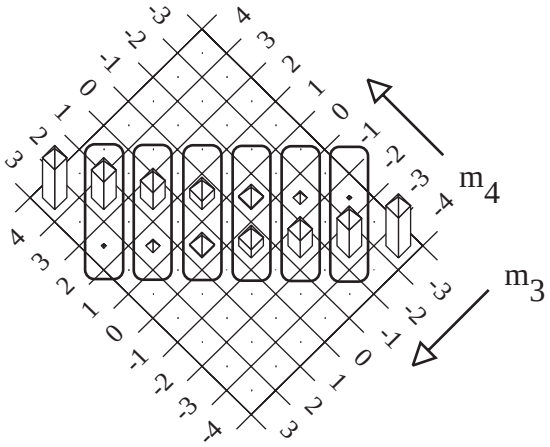

Fig. 29. Calculated relative peak heights for the two components of the odd-numbered resonances, symbolized by the column heights for each pair of m_3 and m_4. For example, the coupling of $|F=3, m_3=1\rangle$ and $|F=4, m_4=2\rangle$ is five times as strong as that of $|F=3, m_3=2\rangle$ and $|F=4, m_4=1\rangle$

7.2 Improvements for future experiments

In order to become competitive with the precision of the literature value the magnetic flux density has to be increased by at least a factor of 100 because at an applied field of only 11 μT the nuclear influence is very small (White et al. used 5 mT [81]). In fact, only because of the precision offered by the technique of phase-locked lasers could the nuclear contribution be detected optically already at these flux densities. It is furthermore important to have a very homogeneous field because small relative inhomogeneities lead to a strong broadening of the dark resonance lines.

A further optimization concerns the angle β between laser propagation direction and the magnetic field. In (87) the relative uncertainties of x_{opt} and a_{opt} enter with equal weights. However, since the influence of a on the peak positions is rather small the uncertainty of a_{opt} is in general larger than that of x_{opt}. Therefore it could be advantageous to increase β above 45° in order to increase the fraction of the total line strength contained in the odd-numbered resonances, leading to an improved fit of a_{opt}. Furthermore, fluctuations of the cell temperature have to be suppressed to below 10 mK in order to eliminate the influence of the buffer gas pressure (Fig. 21). One also has to take a possible sloping background into account because while the laser difference frequency is scanned across the spectrum by changing the current of the slave laser, its output power also increases.

An alternative way of extracting g_I/g_J from a 15-peak spectrum is to compare the resonance frequencies of each pair of adjacent resonances. Each of the 14 pairings gives a pair $(x_{\mathrm{opt}}, a_{\mathrm{opt}})$ which could then be averaged. In this way it will also be possible to check for the presence of drifts (for example, of B) during the measurement of the spectrum.

In the end it might be possible to study in more detail the dependence of g_J on collisions with buffer gas atoms, as discussed in Sect. 5.2.1.

8 Application 3: frequency standard

The narrow coherent population trapping resonance lines can be exploited for an atomic frequency standard. The general idea has already been introduced in Sect. 5.2. The rf oscillator that determines the frequency difference of the phase-locked loop is tuned to a specific point on the dark resonance line shape, for instance the point at half height where the line shape has the steepest slope (in practice one would probably prefer the use of a modulation technique to lock the oscillator to the center of the resonance). Fluctuations in the frequency of the rf oscillator lead to a change in measured signal which can be used by a servo loop to tune the oscillator back to the desired frequency.

Cesium is a particularly attractive candidate for an atomic frequency standard because the SI unit of one second is defined as 9,192,631,770 periods of the 0-0 ground-state hyperfine transition in an unperturbed cesium atom. A standard directly based on that transition is therefore a *primary* standard. Currently the second is realized with cesium atomic beams that are spin-polarized using a magnetic state selector and then interact with a 9.2 GHz rf field in two Ramsey zones separated by about 1 m. For several years the attainable accuracy has been hovering around $1:10^{14}$. Recently state preparation by optical pumping has contributed to an improvement down to a few parts in 10^{15} in the NIST-7 atomic clock at Boulder. The latest developments are clocks based on atomic fountains where instabilities better than 10^{-15} seem realistic in the near future [88].

Instead of using the rf waves directly Ezekiel and coworkers have optically excited and probed the "clock transition" in sodium and cesium atomic beams. For a sodium experiment [3, 49, 89] an electrooptic modulator imposed 1.77-GHz sidebands on a dye laser beam. With a Ramsey zone separation of 15 cm they reached relative frequency fluctuations (Allan standard deviation [90]) of 5.6×10^{-11} at $\tau = 100$ s [3] and 1.5×10^{-11} at $\tau = 1000$ s [89]. In a cesium beam experiment [24] with 15 cm zone separation and a diode laser current-modulated at 4.6 GHz, i.e., half the hyperfine frequency, an instability of $6\times10^{-11}/\sqrt{\tau}$ was projected.

In principle a frequency standard based on a vapor cell would be much more practical because it is not as bulky as an atomic beam machine and is also much easier to shield from external fields. However, the wall coating or the buffer gas that is commonly used to increase the effective interaction time also introduces systematic frequency shifts that have to be characterized and controlled with very high accuracy. In turn, a big problem of Ramsey-type clocks, thermally induced phase shifts between the two zones, would be eliminated.

9 Conclusion

It has been shown that phase-locked lasers allow spectroscopic measurements in atomic vapors with unprecedented accuracy and precision. The experimental technique relies on an electronic servo loop that controls the difference phase of two laser light fields to within fractions of a radian, allowing the preparation of coherent population trapping resonances with extremely narrow linewidths. These resonances have been characterized as a function of experimental parameters.

A theoretical model has been developed that exploits the symmetry properties of cesium atoms under bichromatic excitation on the D_2 line and gives quantitative agreement with the experimental dark-resonance spectra for arbitrary combinations of light polarizations and magnetic field directions. The symmetry considerations greatly simplify the complexity of the problem and allow deeper insight into the physical structure of the coupling between the atomic system and the light fields.

The interaction time of the atoms with the light beams can be increased by adding neon as a buffer gas to the cesium vapor, leading to very narrow resonance linewidths of less than 50 Hz. There are two interesting side effects of the pressure broadening by the buffer gas: the ac Stark effect is strongly reduced, and there is a change in the multipole order of the dominant coupling between atoms and light that can be described quantitatively by the theoretical model.

The narrow lines readily lend themselves to precision measurements:

Magnetometry. dc fields larger than 1 μT can be detected with 3×10^{-5} relative uncertainty, independent of field strength. In first experiments ac flux densities of 7 pT have been detected in 0.5 s integration time. An extrapolation to a signal-to-noise

ratio of unity gives an estimate for the detection limit of the current setup of 500 fT.

g-factor ratio. For a suitable combination of laser polarizations and magnetic field direction the ratio g_I/g_J of nuclear to electronic *g*-factors in cesium atoms can be extracted from the dark resonance spectrum. The precision of a first proof-of-principle measurement can be greatly increased when the experiment is repeated in much stronger magnetic fields. It might be interesting to study g_I/g_J as a function of buffer gas pressure in order to see the onset of collisional modifications of the atomic wavefunctions.

Frequency standard. In a shielded vapor cell the position of the coherent population trapping resonance could be used as a reference for a 9.2-GHz oscillator, thus providing a compact primary frequency standard in the near future.

For all the precision measurements a detailed understanding of systematic effects is essential. Several of these, among them influences of the buffer gas and of laser intensity and detuning, have been studied in detail.

Acknowledgements. Many people have contributed to the results described in this work. We would like to give special thanks to D. Meschede for his continuing support; A. Weis for many stimulating discussions; the Ph.D. and "Diplom" students who contributed to the experiments described here: O. Schmidt, Z. Hussein, S. Brandt, and L. Graf; the visiting scientists A. Naumov, V. Zadkov, and B. Grishanin from Moscow State University, and E. Mariotti and V. Biancalana from Siena University. We also thank C. Affolderbach and S. Knappe for a careful reading of the manuscript. Financial support by the Deutsche Forschungsgemeinschaft, the German Academic Exchange Service, and the Volkswagen Foundation is gratefully acknowledged.

References

1. G. Alzetta, A. Gozzini, L. Moi, G. Orriols: Il Nuovo Cim. **36B**, 5 (1976)
2. A. Aspect, E. Arimondo, R. Kaiser, N. Vansteenkiste, C. Cohen-Tannoudji: Phys. Rev. Lett. **61**, 826 (1988)
3. P.R. Hemmer, S. Ezekiel, C.C. Leiby, Jr.: Opt. Lett. **8**, 440 (1983)
4. M.O. Scully, M. Fleischhauer: Phys. Rev. Lett. **69**, 1360 (1992)
5. M. Fleischhauer, M.O. Scully: Phys. Rev. A **49**, 1973 (1994)
6. S. Brandt, A. Nagel, R. Wynands, D. Meschede: Phys. Rev. A **56**, R1063 (1997)
7. A. Nagel, L. Graf, A. Naumov, E. Mariotti, V. Biancalana, D. Meschede, R. Wynands: Europhys. Lett. **44**, 31 (1998)
8. H.R. Gray, R.M. Whitley, C.R. Stroud, Jr.: Opt. Lett. **3**, 218 (1978)
9. G.P. Agrawal: Phys. Rev. A **24**, 1399 (1981)
10. S.E. Harris, J.E. Field, A. Imamoğlu: Phys. Rev. Lett. **64**, 1107 (1990)
11. A. Kasapi: Phys. Rev. Lett. **77**, 1035 (1996)
12. E. Arimondo: Prog. Opt. **XXXV**, 257 (1996)
13. P.L. Kelley, P.J. Harshman, O. Blum, T.K. Gustafson: J. Opt. Soc. Am. B **11**, 2298 (1994)
14. B.A. Grishanin, V.N. Zadkov, R. Wynands, A. Nagel, D. Meschede: submitted for publication
15. O. Schmidt, R. Wynands, Z. Hussein, D. Meschede: Phys. Rev. A **53**, R27 (1996)
16. M.O. Scully: Phys. Rev. Lett. **67**, 1855 (1991)
17. B.A. Grishanin, V.N. Zadkov, D. Meschede: JETP **86**, 79 (1998); originally appeared in: Zh. Eksp. Teor. Fiz. **113**, 144 (1998)
18. C.E. Wieman, L. Hollberg: Rev. Sci. Instrum. **62**, 1 (1991)
19. K.B. MacAdam, A. Steinbach, C. Wieman: Am. J. Phys. **60**, 1098 (1992)
20. O. Schmidt, K.-M. Knaak, R. Wynands, D. Meschede: Appl. Phys. B **59**, 167 (1994)
21. R. Kallenbach, B. Scheumann, C. Zimmermann, D. Meschede, T.W. Hänsch: Appl. Phys. Lett. **54**, 1622 (1989)
22. D. Leibfried, F. Schmidt-Kaler, M. Weitz, T.W. Hänsch: Appl. Phys. B **56**, 65 (1993)
23. C.J. Myatt, N.R. Newbury, C.E. Wieman: Opt. Lett. **18**, 649 (1993)
24. P.R. Hemmer, M.S. Shahriar, H. Lamela-Rivera, S.P. Smith, B.E. Bernacki, S. Ezekiel: J. Opt. Soc. Am. B **10**, 1326 (1993)
25. K.-J. Ebeling: Ulm University, private communication (1997)
26. R. Wynands, T. Mukai, T.W. Hänsch: Opt. Lett. **17**, 1749 (1992)
27. Th. Udem, A. Huber, B. Gross, J. Reichert, M. Prevedelli, M. Weitz, T.W. Hänsch: Phys. Rev. Lett. **79**, 2646 (1997)
28. L.H. Enloe, J.L. Rodda: Proc. IEEE **53**, 165 (1965)
29. R.C. Steele: Electron. Lett. **19**, 69 (1983)
30. H.E. Hagemeier, S.R. Robinson: Appl. Opt. **18**, 270 (1979)
31. C.L. Hayes, L.M. Laughman: Appl. Opt. **16**, 263 (1977)
32. T. Mukai, R. Wynands, T.W. Hänsch: Opt. Commun. **95**, 71 (1993)
33. H.R. Telle, H. Li: Electron. Lett. **26**, 858 (1990)
34. M. Prevedelli, T. Freegarde, T.W. Hänsch: Appl. Phys. B **60**, S241 (1995)
35. J.L. Hall, Ma Long-Sheng, G. Kramer: IEEE J. Quantum Electron. **QE-23**, 427 (1987)
36. R. Wynands, O. Coste, C. Rembe, D. Meschede: Opt. Lett. **20**, 1095 (1995)
37. T. Ikegami, S. Slyusarev, S. Ohshima, E. Sakuma: Opt. Commun. **127**, 69 (1996)
38. S. Slyusarev, T. Ikegami, S. Ohshima, E. Sakuma: Opt. Commun. **135**, 223 (1997)
39. B. Dahmani, L. Hollberg, R. Drullinger: Opt. Lett. **12**, 876 (1987)
40. H. Li, H.R. Telle: IEEE J. Quantum Electron. **QE-25**, 257 (1989)
41. P. Laurent, A. Clairon, C. Bréant: IEEE J. Quantum Electron. **QE-25**, 1131 (1989)
42. E.A. Korsunsky, W. Maichen, L. Windholz: Phys. Rev. A **56**, 3908 (1997)
43. A.M. Akulshin, A.A. Celikov, V.L. Velichansky: Opt. Commun. **84**, 139 (1991)
44. O. Schmidt: *Dunkelzustände in Cäsiumdampf*, Ph.D. Thesis, Hannover University (1995), in German
45. M. Xiao, Y. Li, S. Jin, J. Gea-Banacloche: Phys. Rev. Lett. **74**, 666 (1995)
46. D. Grischkowsky: Phys. Rev. A **7**, 2096 (1973)
47. R.E. Slusher, H.M. Gibbs: Phys. Rev. A **5**, 1634 (1972)
48. A. Kasapi, M. Jain, G.Y. Yin, S.E. Harris: Phys. Rev. Lett. **74**, 2447 (1995)
49. J.E. Thomas, P.R. Hemmer, S. Ezekiel, C.C. Leiby, Jr., R.H. Picard, C.R. Willis: Phys. Rev. Lett. **48**, 867 (1982)
50. W. Happer: Rev. Mod. Phys. **44**, 169 (1972)
51. D.R. Swenson, L.W. Anderson: Nucl. Instrum. Methods B **29**, 627 (1988)
52. J.H. Xu: Ph.D. Thesis, Pisa University (1994)
53. D.E. Nikonov, U.W. Rathe, M.O. Scully, S.-Y. Zhu, E.S. Fry, X. Li, G.G. Padmabandu, M. Fleischhauer: Quantum Opt. **6**, 245 (1994)
54. S. Ezekiel, S.P. Smith, M.S. Shahriar, P.R. Hemmer: J. Lightwave Technol. **13**, 1189 (1995)
55. G.C. Bjorklund, M.D. Levenson, W. Lenth, C. Ortiz: Appl. Phys. B **32**, 145 (1983)
56. S.W. North, X.S. Zheng, R. Fei, G.E. Hall: J. Chem. Phys. **104**, 2129 (1996)
57. R. Wynands, A. Nagel: in preparation
58. N. Beverini, P. Minguzzi, F. Strumia: Phys. Rev. A **4**, 550 (1971)
59. E. Arimondo: In Fundamentals of Quantum Optics III, Lecture Notes in Physics **420**, ed. by F. Ehlotzky, (Springer, Berlin, Heidelberg 1994) p. 170
60. R. Wynands, A. Nagel, S. Brandt, D. Meschede, A. Weis: Phys. Rev. A **58**, 196 (1998)
61. A.V. Taichenachev, A.M. Tumaikin, V.I. Yudin: JETP **83**, 949 (1996)
62. F.T. Hioe, C.E. Carroll: Phys. Rev. A **37**, 3000 (1988)
63. H. Kanokogi, K. Sakurai: Phys. Rev. A **54**, 2334 (1996)
64. R. Loudon: *The Quantum Theory of Light* (Oxford University Press, Oxford 1983)
65. R. Wynands: Habilitation thesis, Bonn University 1998
66. B. Cagnac, G. Grynberg, F. Biraben: J. Phys. (Paris) **34**, 845 (1973)
67. P.P. Herrmann, J. Hoffnagle, N. Schlumpf, V.L. Telegdi, A. Weis: J. Phys. B: At., Mol. Opt. Phys. **19**, 1271 (1986)
68. K.D. Bonin, T.J. McIlrath: J. Opt. Soc. Am. **1**, 52 (1984)
69. M.A. Yuratich, D.C. Hanna: J. Phys. B: At. Mol. Phys. **9**, 729 (1976)
70. W. Happer, B.S. Mathur: Phys. Rev. **163**, 12 (1967)
71. N. Beverini, F. Strumia, G. Rovera: Opt. Commun. **37**, 394 (1981)

72. R.M. Herman: Phys. Rev. **175**, 10 (1968)
73. H.G. Robinson: NIST Boulder, private communication (1996). The result was part of the thesis work of Staffa
74. M. Kristensen, F.J. Blok, M.A. van Eijkelenborg, G. Nienhuis, J.P. Woerdman: Phys. Rev. A **51**, 1085 (1995)
75. A good overview of the existing theoretical literature is given by B.W. Shore: *The Theory of Coherent Atomic Excitation*, Vol. 2 (Wiley, New York 1990)
76. P.R. Hemmer, M.S. Shahriar, V.D. Natoli, S. Ezekiel: J. Opt. Soc. Am. **6**, 1519 (1989), and references therein
77. M. Hämäläinen, R. Hari, R. Ilmoniemi, J. Knuutila, O.V. Lounasmaa: Rev. Mod. Phys. **65**, 413 (1993)
78. C. Cohen-Tannoudji, J. Dupont-Roc, S. Haroche, F. Laloë: Phys. Rev. Lett. **22**, 758 (1969)
79. E.B. Alexandrov, M.V. Balabas, A.K. Vershovskii, A.E. Ivanov, N.N. Yakobson, V.L. Velichanskii, N.V. Senkov: Opt. Spectrosc. **78**, 292 (1995)
80. H. Becker: Archaeological Prospection **2**, 217 (1995)
81. C.W. White, W.M. Hughes, G.S. Hayne, H.G. Robinson: Phys. Rev. A **7**, 1178 (1973)
82. G. Wäckerle: Stuttgart University, private communication (1997)
83. A.L. Bloom: Appl. Opt. **1**, 61 (1962)
84. M. Fleischhauer, M.O. Scully: Quantum Semiclass. Opt. **7**, 297 (1995)
85. M.A. Bouchiat, C. Bouchiat: J. Phys. (Paris) **35**, 899 (1974)
86. J. Sapirstein: In *Atomic, Molecular & Optical Physics Handbook*, ed. by G.W.F. Drake , (AIP Press, Woodbury 1996) pp. 352
87. C.S. Wood, S.C. Bennett, D. Cho, B.P. Masterson, J.L. Roberts, C.E. Tanner, C.E. Wieman: Science **275**, 1759 (1997)
88. C. Salomon: In 13th International Conference on Laser Spectroscopy, Hangzhou, China, June 1997
89. P.R. Hemmer, G.P. Ontai, A. Rosenberg, S. Ezekiel: In Proceedings of the 39th Annual Frequency Control Symposium, pp. 88 (1985)
90. J.A. Barnes, A.R. Chi, L.S. Cutler, D.J. Healy, D.B. Leeson, T.E. McGunigal, J.A. Mullen, Jr., W.L. Smith, R.L. Snydor, R.F.C. Vessot, G.M.R. Winkler: IEEE Trans. Instrum. Meas. **20**, 105 (1971)